EUROPEAN ORGANIZATION FOR NUCLEAR RESEARCH
European Laboratory for Particle Physics

Internal NOTE
ALICE Reference Number
2009-035
date of last change
November 19, 2009

Alignment of the ALICE Inner Tracking System with cosmic-ray tracks

C. Bombonati [a,b], C. Cheshkov [b], A. Dainese [c,1)], C.E. Garcia Trapaga [d,e],
R. Grosso [a], A. Jacholkowski [f], M. Lunardon [a], M. Masera [g], S. Moretto [a],
F. Prino [e], A. Rossi [h], R. Shahoyan [b], M. van Leeuwen [i], and N. Vermeer [i]

[a] Università degli Studi di Padova and INFN, Padova, Italy
[b] CERN, Geneva, Switzerland
[c] INFN - Sezione di Padova, Padova, Italy
[d] InSTEC, Havana, Cuba
[e] INFN - Sezione di Torino, Torino, Italy
[f] Università di Catania, Catania, Italy
[g] Università di Torino and INFN, Torino, Italy
[h] Università di Trieste and INFN, Trieste, Italy
[i] Universiteit Utrecht, Utrecht, the Netherlands

Abstract

The ALICE Inner Tracking System (ITS) consists of six cylindrical layers of silicon detectors with three different technologies; in the outward direction: two pixel, two drift and two strip layers. The number of parameters to be determined in the spatial alignment of the 2198 sensor modules of the ITS is about 13,000. The target alignment precision is well below 10 μm in some cases (pixels). The sources of alignment information are the survey measurements and the reconstructed tracks from cosmic rays and from proton–proton collisions. The main track-based alignment method uses the Millepede global approach. An iterative local method was developed and used as well. We present the results obtained for the ITS alignment using about 10^5 charged tracks from cosmic rays that have been collected during summer 2008, with the ALICE solenoidal magnetic field switched off.

---

1) e-mail: andrea.dainese@pd.infn.it

1 Introduction

The ALICE experiment [1] will study nucleus–nucleus, proton–proton and proton–nucleus collisions at the CERN Large Hadron Collider (LHC). The main physics goal of the experiment is to investigate the properties of strongly-interacting matter in the conditions of high energy density (> 10 GeV/fm^3) and high temperature ($\gtrsim 0.2$ GeV), expected to be reached in central Pb–Pb collisions at $\sqrt{s_{\rm NN}} = 5.5$ TeV. Under these conditions, according to lattice QCD calculations, quark confinement into colourless hadrons should be removed and a deconfined Quark–Gluon Plasma should be formed [2]. In the past two decades, experiments at CERN-SPS ($\sqrt{s_{\rm NN}} = 17.3$ GeV) and BNL-RHIC ($\sqrt{s_{\rm NN}} = 200$ GeV) have gathered ample evidence for the formation of this state of matter [3].

The ALICE experimental apparatus consists of two main components: the central barrel and the forward muon spectrometer. The coverage of the central barrel detectors allows the tracking of particles emitted on a pseudo-rapidity range $|\eta| < 0.9$ over the full azimuth. These detectors are embedded in the large L3 magnet that provides a solenoidal field B = 0.5 T.

The Inner Tracking System (ITS) is a barrel-type silicon tracker that surrounds the interaction region. It consists of six cylindrical layers, with radii between 3.9 cm and 43.0 cm, covering the pseudo-rapidity range $|\eta| < 0.9$. The two innermost layers are equipped with Silicon Pixel Detectors (SPD), the two intermediate layers are made of Silicon Drift Detectors (SDD), while Silicon Strip Detectors (SSD) are mounted on the two outermost layers. The main task of the ITS is to provide precise track and vertex reconstruction close to the interaction point. In particular, the ITS was designed with the aim to improve the position, angle, and momentum resolution for tracks reconstructed in the Time Projection Chamber (TPC), to identify the secondary vertices from the decay of hyperons and heavy flavoured hadrons, to reconstruct the interaction vertex with a resolution better than 100 μm, and to recover particles that are missed by the TPC (due to either dead regions or low-momentum cut-off). The measurement of charm and beauty hadron production in Pb–Pb collisions at the LHC is one of the main items of the ALICE physics program, because it will allow to investigate the mechanisms of heavy-quark propagation and hadronization in the hot and dense medium formed in high-energy heavy-ion collisions and it will serve as a reference for the study of the medium effects on quarkonia [4]. The separation, from the interaction vertex, of the decay vertices of heavy flavoured hadrons, which have mean proper decay lengths $c\tau \sim 100$–500 μm, requires a resolution on the track impact parameter (distance of closest approach to the vertex) well-below 100 μm. This requirement is met by the ITS. According to the design parameters, the position resolution at the primary vertex in the plane transverse to the beam-line for charged-pion tracks reconstructed in the TPC and in the ITS is expected to be approximately, in μm, $10 + 53/(p_{\rm t}\sqrt{\sin\theta})$, where $p_{\rm t}$ is the transverse momentum in GeV/c and θ is the polar angle with respect to the beam-line [4]. However, when considering the real detector, as installed in the experiment, the resolution is in general significantly degraded by the *misalignment*. The ITS is made of thousands of separate modules, whose positions are displaced, with respect to the ideal case, during the assembly and the integration of the different components. These displacements, if not taken into account, degrade the tracking performance of the detector, thus the physics performance. Therefore, it is mandatory to align the detector, that is, to measure the displacements (translations and rotations), so that they can be properly taken into account during track reconstruction. The ITS alignment procedure starts from the positioning survey measurements performed during the assembly, and is refined using tracks from cosmic-ray muons and from particles produced in LHC pp

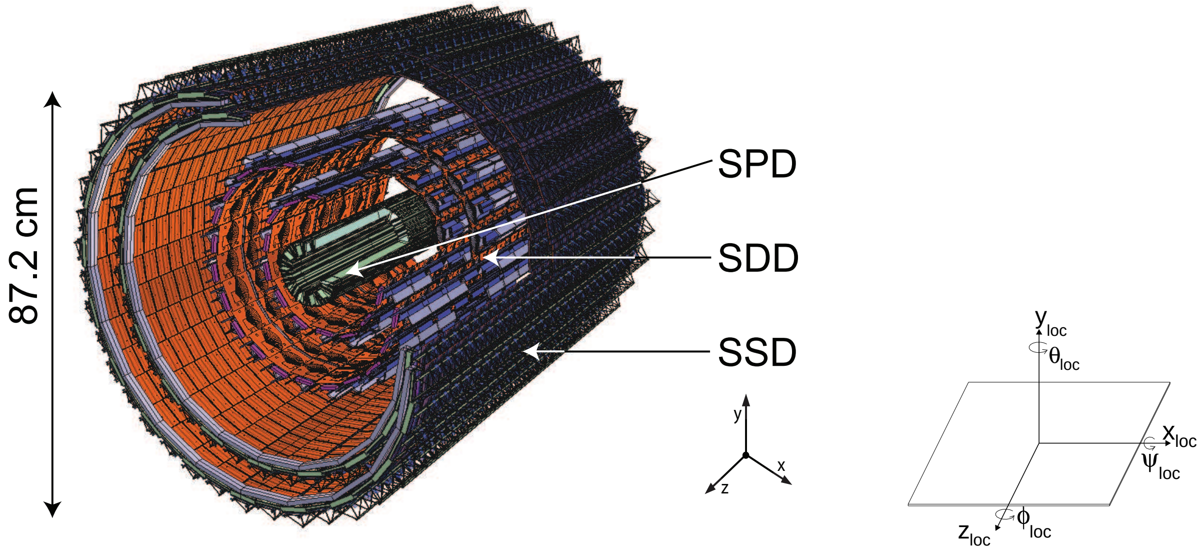

Figure 1: Layout of the ITS and definition of the ALICE global (left) and ITS-module local (right) reference systems.

collisions. Two independent methods, based on tracks-to-measured-points residuals minimization, are considered. The first method uses the Millepede approach [5], where a global fit to all residuals is performed, extracting all the alignment parameters simultaneously. The second method performs a (local) minimization for each single module and accounts for correlations between modules by iterating the procedure until convergence is reached.

In this report, we present the alignment methods for the ITS and the results obtained using the cosmic-data sample collected during summer 2008 with $B = 0$ (a small data set with $B = \pm 0.5$ T was also collected; we used it for a few specific validation checks). In section 2 we describe in detail the ITS detector layout and in section 3 we discuss the strategy adopted for the alignment. In section 4 we describe the 2008 sample of cosmic-muon data. These data were used to validate the available survey measurements (section 5) and to apply the track-based alignment algorithms: the Millepede method (section 6) and a local method that we are developing (section 7). We draw conclusions in section 8.

2 ITS detector layout

The geometrical layout of the ITS layers is shown in the left-hand panel of Fig. 1, as it is implemented in the ALICE simulation and reconstruction software framework (AliRoot [6]). The ALICE global reference system has the z axis on the beam-line, the x axis in the LHC (horizontal) plane, pointing to the centre of the accelerator, and the y axis pointing upward. The axis of the ITS barrel coincides with the z axis. The module local reference system (Fig. 1, right) is defined with the $x_{\rm loc}$ and $z_{\rm loc}$ axes on the sensor plane and the $z_{\rm loc}$ axis in the same direction as the global z axis. The local x direction is approximately equivalent to the global $r\varphi$. The alignment degrees of freedom of the module are translations in $x_{\rm loc}$, $y_{\rm loc}$, $z_{\rm loc}$, and rotations by angles $\psi_{\rm loc}$, $\theta_{\rm loc}$, $\varphi_{\rm loc}$, about the $x_{\rm loc}$, $y_{\rm loc}$, $z_{\rm loc}$ axes, respectively1).

The ITS geometry in AliRoot is described in full detail, down the level of all mechanical structures and single electronic components, using the ROOT [7] geometrical

---

1) The alignment transformation can be expressed equivalently in terms of the local or global coordinates.

Table 1: Characteristics of the six ITS layers.

Layer	Type	r [cm]	$\pm z$ [cm]	Number of modules	Active Area per module $r\varphi \times z$ [mm^2]	Resolution $r\varphi \times z$ [μm^2]	Material budget X/X_0 [%]
1	pixel	3.9	14.1	80	12.8×70.7	12×100	1.14
2	pixel	7.6	14.1	160	12.8×70.7	12×100	1.14
3	drift	15.0	22.2	84	70.17×75.26	35×25	1.13
4	drift	23.9	29.7	176	70.17×75.26	35×25	1.26
5	strip	38.0	43.1	748	73×40	20×830	0.83
6	strip	43.0	48.9	950	73×40	20×830	0.86

modeler. This detailed geometry is used in Monte Carlo simulations and in the track reconstruction procedures, which account for the exact position of the sensor modules and of all the passive material that determine particle scattering and energy loss.

The number, position and segmentation of the ITS layers, as well as the detector technologies, have been optimized according to the requirements of:

- Efficient track finding in the environment of the high particle multiplicity predicted for central Pb–Pb collisions at LHC, which was estimated up to 8000 particles per unit of rapidity at the time of ALICE design. This calls for high granularity in order to keep the system occupancy at the level of a few per cent on all the ITS layers.
- High resolution on track impact parameter and momentum. The momentum and impact parameter resolution for low-momentum particles are dominated by multiple scattering effects in the material of the detector; therefore the amount of material in the active volume has been kept to a minimum. Moreover, for track impact parameter and vertexing performance, it is important to have the innermost layer as close as possible to the beam axis. The innermost SPD layer is located at an average radial distance of 9 mm from the beam vacuum tube.
- Possibility to use the ITS also as a standalone spectrometer, able to track and identify particles down to momenta below 200 MeV/c. For this reason, the four layers equipped with SDD and SSD provide also particle identification capability via dE/dx measurement.

The geometrical parameters of the layers (radial position, length along beam axis, number of modules, spatial resolution, and material budget) are summarized in Table 1. As far as the material budget is concerned, it should be noted that the values reported in Table 1 account for sensor, electronics, cabling, support structure and cooling for particles crossing the ITS perpendicularly to the detector surfaces. Another 1.30% of radiation length comes from the thermal shields and supports installed between SPD and SDD barrels and between SDD and SSD barrels, thus making the total material budget for perpendicular tracks equal to 7.18% of X_0.

In the following paragraphs, the features of each of the three sub-detectors (SPD, SDD and SSD) that are relevant for alignment issues are described (for more details see [1]). We show here, in Fig. 2, the hierarchical structure of the three subsystems, which drives the definition of the alignment procedure (sections 6 and 7). Each of the objects itemized in Fig. 2 is implemented as an *alignable volume* in the software geometry and it can be moved, to account for the misalignment, by applying a transformation defined by the six independent alignment degrees of freedom (three translations and three rotations)

ITS barrel		
SPD barrel	SDD-SSD barrel	
	SDD barrel	SSD barel
Sectors (10)	Layers (2)	Layers (2)
Half-staves (4 on inner, 8 on outer layer)	Ladders (14 on inner, 22 on outer layer)	Ladders (34 on inner, 38 on outer layer)
Modules (2)	Modules (6 on inner, 8 on outer ladders)	Modules (22 on inner, 25 on outer ladders)

Figure 2: Schematic description of the hierarchical structure of the ITS.

of the volume [8].

2.1 Silicon Pixel Detector

The basic building block of the ALICE SPD is a module consisting of a two-dimensional sensor matrix of reverse-biased silicon detector diodes bump-bonded to 5 front-end chips. The sensor matrix consists of 256 × 160 cells, each measuring 50 μm ($r\varphi$) by 425 μm (z). The active area of each module is 12.8 mm ($r\varphi$) × 70.7 mm (z), the thickness of the sensor is 200 μm, while the readout chip is 150 μm thick. Two modules are mounted together along the z direction to form a 141.6 mm long half-stave. Two half-staves are attached head-to-head along the z direction to a carbon-fibre support sector, which provides also cooling. Each sector (see Fig. 3) supports six staves: two on the inner layer and four on the outer layer. The assembly of half-staves on sectors provides an overlap of about 2% of the sensitive areas along $r\varphi$, while there is no sensor overlap along z, where instead there is a small gap between the two half-staves. Five sectors are then mounted together to form an half-barrel and finally the two (top and bottom) half-barrels are mounted around

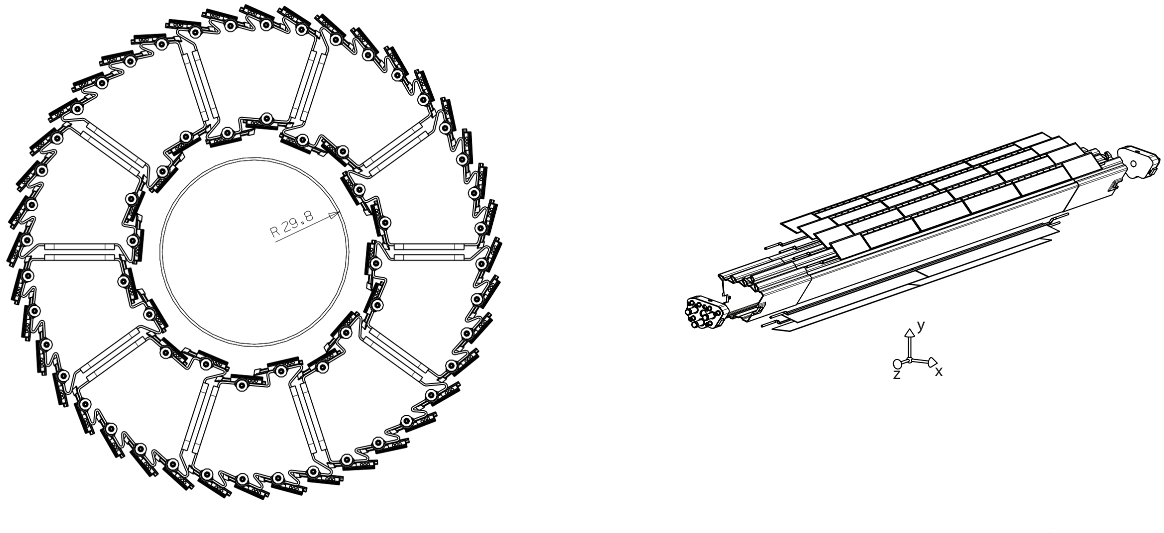

Figure 3: SPD drawings. Left: the SPD barrel and the beam pipe (radius in mm). Right: a Carbon Fibre Support Sector.

the beam pipe to close the full barrel, which is actually composed of 10 sectors. In total, the SPD includes 60 staves, consisting of 240 modules with 1200 readout chips for a total of 9.8×10^6 cells.

The spatial precision of the SPD sensor is determined by the pixel cell size and by the track incidence angle on the detector, as well as by the threshold applied in the readout electronics. The values of resolution along $r\varphi$ and z extracted from beam tests are 12 and 100 μm, respectively.

During the summer 2008 data taking, 212 out of 240 SPD modules were active. A typical threshold value was about 2800 electrons. Noisy pixels, corresponding to less than 0.15%, were masked out and the information was stored in the Offline Conditions DataBase (OCDB) to be used in the offline reconstruction.

2.2 Silicon Drift Detector

The basic building block of the ALICE SDD is a module with a sensitive area of $70.17(r\varphi) \times 75.26(z)$ mm^2, divided into two drift regions where electrons move in opposite directions under a drift field of ≈ 500 V/cm (see Fig. 4, right). The SDD modules are mounted on linear structures called ladders. There are 14 ladders with six modules each on the inner SDD layer (layer 3), and 22 ladders with eight modules each on the outer SDD layer (layer 4). Modules and ladders are assembled to have an overlap of the sensitive areas larger than 580 μm in the both $r\varphi$ and z directions, so as to provide full angular coverage (Fig. 4, left).

The modules are attached with ryton pins to the ladder space frame, which is a lightweight truss made of Carbon-Fibre Reinforced Plastic (CFRP) with a protective coating against humidity absorption, and have their anode rows parallel to the ladder axis (z). During the assembling phase, the positions of the detectors were measured with respect to reference ruby spheres, glued to the ladder feet. The ladders are mounted on a CFRP structure made of a cylinder, two cones and four support rings. The cones provide the links to the outer SSD barrel and have windows for the passage of the SDD services. The support rings are mechanically fixed to the cones and bear reference ruby spheres for

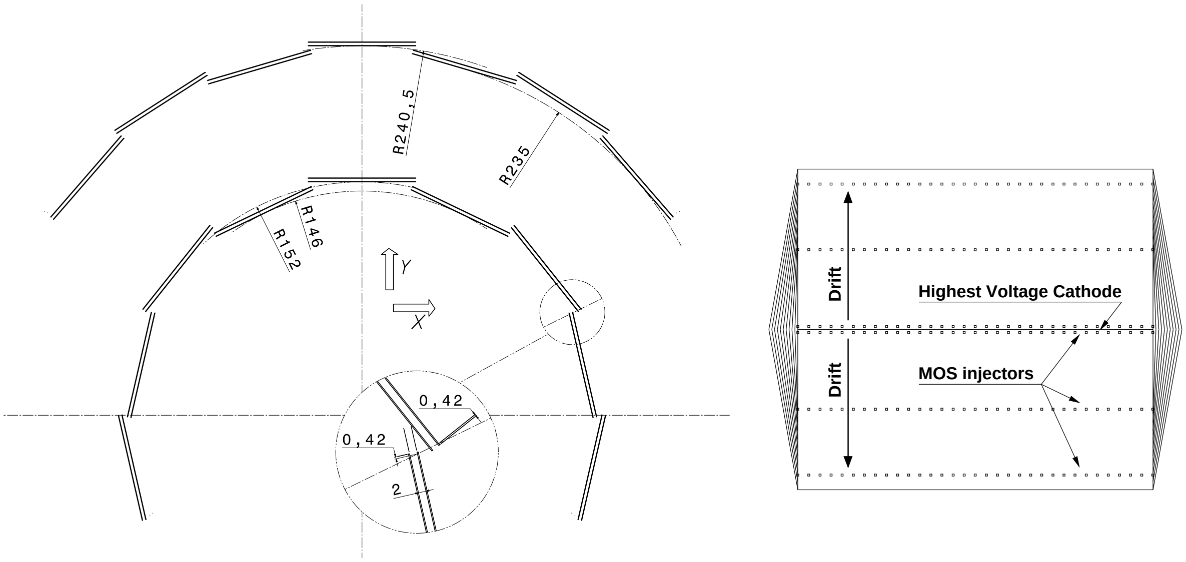

Figure 4: Left: scheme of the SDD layers. Right: scheme of an SDD module. Units are millimeters.

the ladder positioning.

The z coordinate is reconstructed from the centroid of the collected charge along the anodes. The position along the drift coordinate ($x_{\mathrm{loc}} \approx r\varphi$) is reconstructed starting from the measured drift time with respect to the trigger time. An unbiased reconstruction of the x_{loc} coordinate requires therefore to know with good precision the drift speed and the time-zero (t_0), which is the measured drift time for particles with zero drift distance. The drift speed depends on temperature (as $T^{-2.4}$) and it is therefore sensitive to temperature gradients in the SDD volume and to temperature variations with time. Hence, it is important to calibrate frequently this parameter during the data taking. For this reason, in each of the two drift regions of an SDD module, 3 rows of 33 MOS charge injectors are implanted at known distances from the collection anodes [10], as sketched in Fig. 4 (right): when a dedicated calibration trigger is received, the injector matrix provides a measurement of the drift speed in 33 positions along the anode coordinate for each SDD drift region. Finally, a correction for non-uniformity of the drift field (due to non-linearities in the voltage divider and, for a few modules, also due to significant inhomogeneities in dopant concentration) has to be applied: it is extracted from measurements of the systematic deviations between charge injection position and reconstructed coordinates that was performed on all the 260 SDD modules with an infrared laser [11].

The space precision of the SDD detectors, as obtained during beam tests of full-size prototypes, is on average 35 μm along the drift direction x_{loc} and 25 μm for the anode coordinate z_{loc}.

During summer 2008, 246 out of 260 SDD modules participated in data acquisition. The baseline, gain and noise for each of the 133,000 anodes were measured every $\approx$ 24 hours by means of dedicated calibration runs that allowed us also to tag noisy ($\approx$ 0.5%) and dead ($\approx$ 1%) channels. The drift speeds were measured with dedicated injector runs collected every $\approx$ 6 hours and stored in the OCDB and successively used in the reconstruction.

2.3 Silicon Strip Detector

The basic building block of the ALICE SSD is a module composed of one double-sided strip detector connected to two hybrids hosting the front-end electronics. The sensors are 300 μm thick and have an active area of 73×40 mm^2 along z and $r\varphi$ directions, respectively. Each sensor has 768 strips on each side with a pitch of 95 μm. The stereo angle is 35 mrad, which is a compromise between stereo view and reduction of ambiguities resulting from high particle densities. The strips are almost parallel to the beam axis (z-direction), to provide the best resolution in the $r\varphi$ direction. The angle of the strips with respect to the beam axis is +7.5 mrad on one side and −27.5 mrad on the other side. As a result, each strip crosses about 14 strips on the other detector side.

The modules are assembled on ladders of the same design as those supporting the

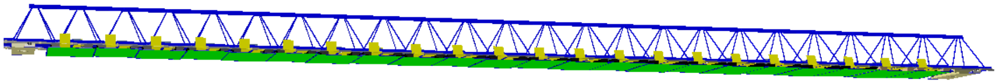

Figure 5: View of one SSD ladder (from layer 5) as described in the AliRoot geometry.

SDD (see Fig. 5). The innermost SSD layer (layer 5) is composed of 34 ladders, each of them being a linear array of 22 modules along the beam direction. Layer 6 (the outermost ITS layer) consists of 38 ladders, each made of 25 modules. In order to obtain full pseudorapidity coverage, the modules are mounted on the ladders with small overlaps between successive modules, that are 600 μm apart in the radial direction. The 72 ladders, carrying a total of 1698 modules, are mounted on Carbon Fibre Composite support cones in two cylinders. Carbon fiber is lightweight (to minimize the interactions) and at the same time it is a stiff material allowing to minimize the bending due to gravity. The ladders are 120 cm long, but the sensitive area on layer 5 amounts 88 cm and on layer 6 it amounts 100 cm. For each layer, the ladders are mounted at two slightly different radii ($\Delta r = 6$ mm) such that full azimuthal coverage is obtained. The acceptance overlaps, present both along z and $r\varphi$, amount to 2% of the SSD sensor surface. The positions of the sensors with respect to reference points on the ladder were measured during the detector construction phase, as well as the ones of the ladders with respect to the support cones.

The spatial resolution of the SSD system is determined by the 95 μm pitch of the sensor readout strips and the charge-sharing between those strips. Without making use of the analogue information the r.m.s spatial resolution is 27 μm. Beam tests have shown that a spatial resolution of better than 20 μm in the rφ direction can be obtained by analyzing the charge distribution within each cluster. In the direction along the beam, the spatial resolution is of about 830 μm.

During the 2008 cosmic run, 1477 out of 1698 SSD modules took data. The fraction of bad strips was $\approx$1.5%. The SSD gain calibration has two components: overall calibration of ADC values to energy loss and relative calibration of the P and N sides. This charge matching is a strong point of double sided silicon sensors and helps to remove fake clusters. Both calibrations relied on cosmics. The resulting normalized difference in P- and N-charge has a FWHM of 11%. The gains have proved to be stable during the data taking. In any case, since the signal-to-noise ratio is larger than 20, the detecting efficiency does not depend much on the details of the gain calibration.

3 Alignment target and strategy

For silicon tracking detectors, the ‘standard’ target of the alignment procedures is the achievement a level of precision and accuracy such that the resolution on the reconstructed track parameters (in particular, the impact parameter and the curvature, which measures the transverse momentum) is degraded by at most 20% with respect to the resolution expected in case of the ideal geometry without misalignment. This standard is adopted by all four LHC experiments.

The resolutions on the track impact parameter and curvature are both proportional to the space point resolution, in the limit of negligible multiple scattering effect (large momentum). If the residual misalignment is assumed to be equivalent to random gaussian spreads in the six alignment parameters of the sensor modules, on which space points are measured, a 20% degradation in the effective space point resolution (hence 20% degradation of the track parameters in the large momentum limit) is obtained when the misalignment spread in a given direction is $\sqrt{120\%^2 - 100\%^2} \approx 70\%$ of the intrinsic sensor resolution along that direction. With reference to the intrinsic precisions listed in Table 1, the target residual misalignment spreads in the local coordinates on the sensor plane are: for SPD, 8 μm in x_{loc} and 70 μm in z_{loc}; for SDD, 25 μm in x_{loc} and 18 μm in z_{loc}; for SSD, 14 μm in x_{loc} and 500 μm in z_{loc}. Since also the misalignment in the θ_{loc} angle (rotation about the axis normal to the sensor plane) impacts directly on the effective spatial precision, the numbers given above should be taken as effective spreads including also the effect of the $\theta_{\rm loc}$ rotation. In any case, these target numbers are only an indication of the precision that is requested from the alignment procedures.

The other alignment parameters ($y_{\rm loc}$, $\psi_{\rm loc}$, $\varphi_{\rm loc}$) describe movements of the modules mainly in the radial direction. These have a small impact on the effective resolution, for tracks with a small angle with respect to the normal to the module plane, a typical case for tracks coming from the interaction region. However, they are related to the so-called *weak modes*: correlated misalignments of the different modules that do not affect the reconstructed tracks fit quality (χ^2), but bias systematically the track parameters. A typical example is radial expansion or compression of all the layers, which biases the measured track curvature, hence the momentum estimate. Correlated misalignments for the parameters on the sensor plane ($x_{\rm loc}$, $z_{\rm loc}$, $\theta_{\rm loc}$) can determine weak modes as well. These misalignments are, by definition, difficult to determine with tracks from collisions, but can be tackled using physical observables [12] (e.g. looking for shift in invariant masses of reconstructed decay particles) and cosmic-ray tracks. These offer a unique possibility to correlate modules that are never correlated in case of tracks from the interaction region, and they offer a broad range of track-to-module-plane incidence angles that help to constrain also the $y_{\rm loc}$, $\psi_{\rm loc}$ and $\varphi_{\rm loc}$ parameters, thus improving the sensitivity to weak modes.

As already mentioned in the introduction, the sources of alignment information that we use are the survey measurements and the reconstructed space points from cosmic-ray and collision particles. These points are the input for the software alignment methods, based on global or local minimization of the residuals. The strategy for the ITS first alignment is outlined as follows:

1. Validation of the SSD survey measurements with cosmic-ray tracks.
2. Alignment of SPD and SSD with cosmic-ray tracks, without magnetic field. The initial alignment is more robust if performed with straight tracks (no field), which help to avoid possible biases that can be introduced when working with curved tracks (e.g. radial layer compression/expansion).
3. Use of the already aligned SPD and SSD to confirm and refine the initial time-zero calibration of SDD, obtained with SDD standalone methods.
4. Validation of the SDD survey measurements with cosmic-ray tracks.
5. Alignment of the full detector (SPD, SDD, SSD) with cosmic-ray tracks, including also data collected with magnetic field B = 0.5 T. These data are extremely useful also to study the track quality and precision as a function of the measured track momentum, which allows to separate the detector resolution and residual misalignment from the multiple scattering effect.
6. Alignment with tracks from pp collisions, with both B = 0 and B = 0.5 T. Cosmic-ray tracks have a dominant vertical component and the sides of the barrel layers have limited statistics. In addition, most of the tracks crossing the side modules, which are close to vertical, have small incidence angles with respect to the module plane. We reject tracks with incidence angle below 30°, because the precision of the corresponding space points is much worse than for other tracks and it is quite difficult to evaluate and account for. For this reason, tracks from pp collisions are essential to complete the alignment of the full detector. They will also be used to routinely monitor the quality of the alignment during data taking, and refine the corrections if needed.
7. Relative alignment of the ITS and the TPC, when both detectors are already inter-

nally aligned and calibrated. This relative alignment will be performed using tracks from pp collisions. Relative movements of the two detectors are monitored by a dedicated system based on lasers, mirrors and cameras [13].

This report covers the steps 1 and 2, with an outlook on step 3.

4 Cosmic-ray run 2008: data taking and reconstruction

During the 2008 cosmic run, extending from June to October, about 10^5 events with reconstructed tracks in the ITS have been collected. In order to simplify the first alignment round, the solenoidal magnetic field was switched off during most of this data taking period. Two types of cosmic triggers were available in 2008: a trigger provided by the ACORDE detector (dedicated to the cosmic ray studies), and a trigger provided by the SPD. ACORDE [1] is a large surface scintillator array, covering about 10% (20 m^2) of the three upper octants of the ALICE magnet, which provides a relatively high ($\approx$ 100 Hz) cosmic trigger rate. This trigger is useful for the main tracking detector, the TPC, whose geometrical dimension matches well that of ACORDE. On the other hand, for a small inner detector like the ITS, this trigger has a low purity level (below 1%) in terms of the number of events with tracks crossing all its layers. For these reasons, using the SPD trigger (described in the following) was much more convenient for the purpose of collecting events for the ITS alignment, and the ACORDE triggered events were not used. The SPD FastOR trigger [1] is based on a programmable hit pattern recognition system (on FPGA) at the level of individual readout chips (1200 in total, each reading a sensor area of about 1.4×1.4 cm^2). This trigger system enables a flexible selection of events of interest, for example high-multiplicity proton–proton collisions, foreseen to be studied in the scope of the ALICE physics program. For the 2008 cosmic run, the trigger logic consisted in selecting events with at least one hit on the upper half of the outer SPD layer ($r \approx 7$ cm) and at least one on the lower half of the same layer. This trigger condition enhances significantly the probability of selecting events in which a cosmic muon, coming from above (the dominant component of the cosmic-ray particles reaching the ALICE cavern placed below $\approx$ 30 m of molasse), traverses the full ITS detector. This FastOR trigger is very efficient (more than 99%) and has purity (fraction of events with a reconstructed track having points in both SPD layers) reaching about 30–40%, limited mainly by the radius of the inner layer ($\approx$ 4 cm) because the trigger assures only the passage of a particle through the outer layer ($\approx$ 7 cm). For the FastOR trigger, typically 77% of the chips (i.e. about 90% of the active modules) could be configured and used. The trigger rate was about 0.18 Hz. The average SPD FastOR trigger rate scales geometrically quite well with the ACORDE trigger rate and is also in agreement with the known cosmic-muon flux in ALICE, as measured by the L3 experiment [14] at LEP, that was installed in the same cavern.

The following procedure, fully integrated in the AliRoot framework [6], is used for track reconstruction:

- the event reconstruction starts from the cluster finding in the ITS (hereafter, we will refer to the clusters as “points”);
- a pseudo primary vertex is created using the reconstructed points in the two SPD layers; this is done by searching for a set of at least three points lying on a straight line and defining as vertex the middle point of the segment between the two points that belong to the same layer; in this way the rest of reconstruction can proceed in a similar way as for interactions occurring inside the beam pipe; if there are less than the required three points in SPD, also the SDD and SSD points can be used

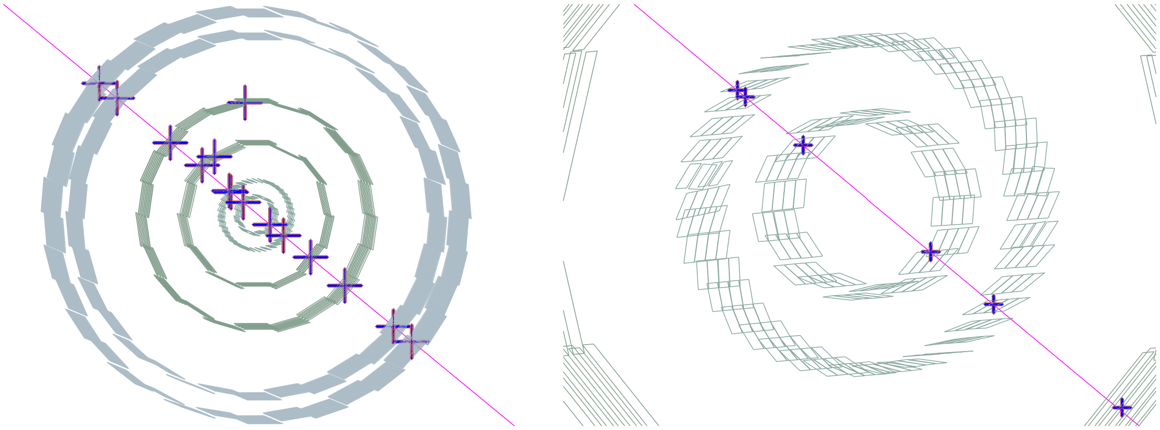

Figure 6: (colour online) A clean cosmic event reconstructed in the ITS (left), as visualized in the ALICE event display. The zoom on the SPD (right) shows an “extra” point in one of the $r\varphi$ acceptance overlaps of the outer layer.

in the vertex construction process;

- track reconstruction is performed using the ITS standalone tracker (as described in [15, 4]), which finds tracks in the outward direction, from the innermost SPD layer to the outermost SSD layer, using the previously found pseudo primary vertex as a seed; all tracks found in this way are then refitted using the standard Kalman-filter fit procedure as implemented in the default ITS tracker.

During the track refit stage, when the already identified ITS points are used in the Kalman-filter fit in the inward direction, in order to obtain the track parameters estimate at the (pseudo) vertex, “extra” points are searched for in the ITS module overlaps. For each layer, a search road for these overlap points in the neighbouring modules is defined with a size of about seven times the current track position error. Currently, the “extra” points are not used to update the track parameters, so they can be exploited as a powerful tool to evaluate the ITS alignment quality.

A clean cosmic event consists of two separate tracks, one “incoming” in the top part of the ITS and one “outgoing” in the bottom part. Their matching at the reference median plane ($y = 0$) can be used as another alignment quality check. These two track halves are merged together in a single array of track points, which is the single-event input for the track-based alignment algorithms. A typical such event, as visualized in the ALICE event display, is shown in Fig. 6.

The uncorrected zenith-azimuth 2D distribution of the (merged) tracks with at least eight points in the ITS is shown in Fig. 7, where the azimuth angle is defined in a horizontal plane starting from the positive side of the z global axis. The modulations in the azimuthal dependence of the observed flux are due to the presence of inhomogeneities in the molasse above the ALICE cavern, mainly the presence of two access shafts. These are seen as the structures at zenith angle $\approx 30°$ and azimuth $\approx 180°$ (large shaft) and $\approx 270°$ (small shaft). On top of these structures, the effect of the SPD outer layer geometrical acceptance is visible: the azimuthal directions perpendicular to the z axis (around 90° and 270°) have larger acceptance in the zenith angle.

Figure 8 shows the coverage of the ITS modules for the sample of cosmic events used for alignment: number of track points in (φ, z) plane, where each cell corresponds approximately to a module, for the outer layers of SPD, SDD, SSD. The figure illustrates

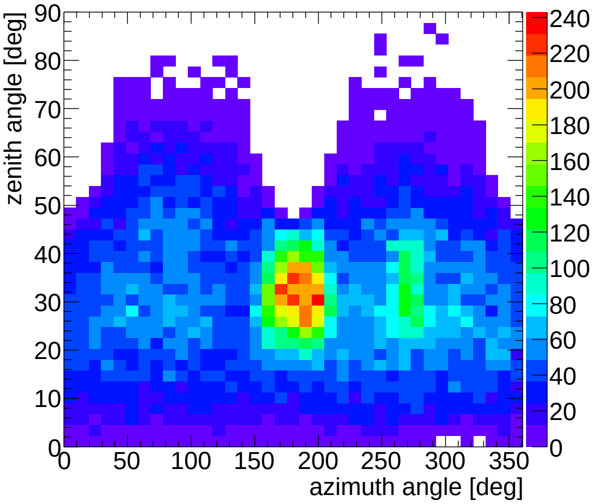

Figure 7: (colour online) Uncorrected distribution of the zenith-azimuth angles of the cosmic tracks reconstructed in the ITS.

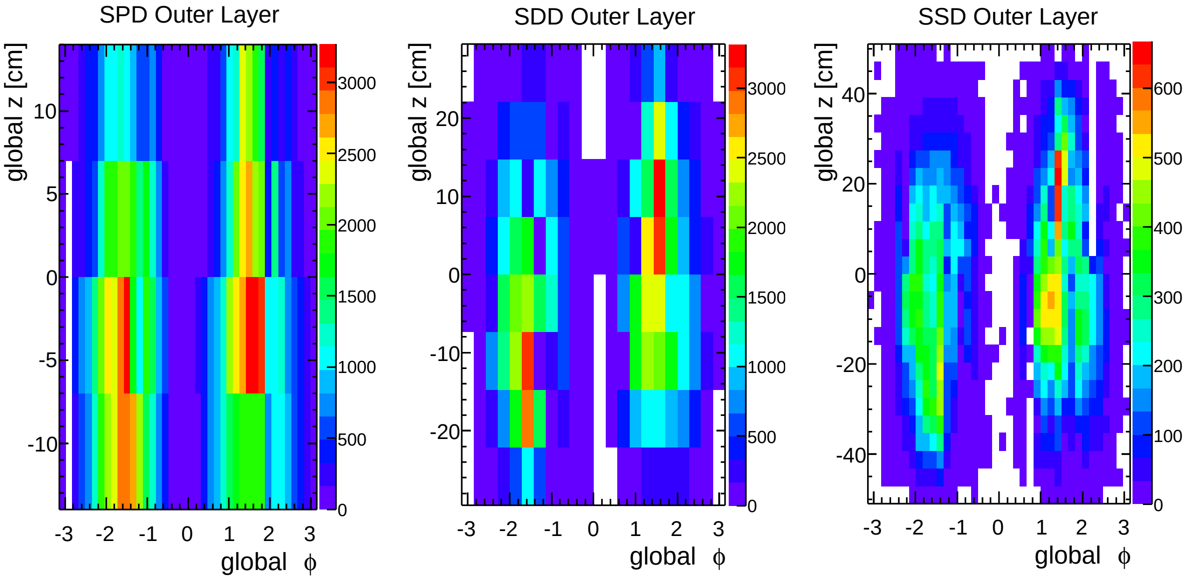

Figure 8: (colour online) 2008 cosmics sample, B = 0: total number of points associated to tracks per module, for the outer layers of SPD, SDD, and SSD.

the limitation of the usage of cosmic-ray tracks for the alignment of a cylindrical detector like the ITS: because of the small size of the triggering detector (SPD), the dominance of small zenith angles for cosmic-ray particles and the necessary cut on the track-to-module incidence angle, the occupancy of the side modules is small, especially for the external layers.

5 Validation of the survey measurements

The SDD and SSD were surveyed during the assembling phase using a measuring machine. The survey, very similar for the two detectors, was carried out in two stages: the measurement of the positions of the modules on the ladders and the measurement of the positions of the ladder endpoints on the support cone.

In the first stage, for SDD for example [16], the three-dimensional positions of six reference markers engraved on the detector surface were measured for each module with respect to a reference system defined from ruby spheres fixed to the support structure. The precision of the measuring machine was 5 μm in the coordinates on the ladder plane and about 10 μm in the direction orthogonal to the plane. The deviations of the reference marker coordinates on the plane with respect to design positions showed an average value of 1 μm and a r.m.s. of 20 μm. In the second stage, the positions of the ladder end points with respect to the cone support structure were measured with a precision of about 10 μm. However, for the outer SSD layer, the supports were dismounted and remounted after the survey; the precision of the remounting procedure is estimated to be around 20 μm in the $r\varphi$ direction [1].

In the following we describe the results for the validation of the SSD survey measurements with cosmic-ray data. The validation of the SDD survey will be performed after completion of the detector calibration.

5.1 Double points in SSD module overlaps

As already mentioned, the modules are mounted with a small (2 mm) overlap in both the longitudinal (z, modules on the same ladder) and transverse directions ($r\varphi$, adjacent ladders). These overlaps allow us to verify the relative position of neighbouring modules using double points produced by the same particle on the two modules. More precisely, they allow to estimate the effective spatial resolution of the sensor modules, i.e. the combination of the intrinsic spatial resolution and the relative misalignment of the two adjacent modules. Since the two points are very close in space and the amount of material crossed by the particle in-between the two points is very limited, multiple scattering can be neglected.

We define the distance $\Delta x_{\rm loc}$ between the two points in the local x direction on the module plane ($\approx r\varphi$) by projecting, along the track direction, the point of one of the two modules on the other module plane.

Figure 9 shows the $\Delta x_{\rm loc}$ distributions without and with the survey corrections, for the two SSD layers. When the survey corrections are applied, the spread of the distributions, obtained from a gaussian fit, is $\sigma \approx 25.5$ μm. This arises from the combined spread of the two points, thus the effective position resolution for a single point is estimated to be smaller by a factor $1/\sqrt{2}$, i.e. ≈ 18 μm, which is compatible with the expected intrinsic spatial resolution of about 20 μm. This indicates that the residual misalignment after applying the survey is comparable to zero, or, better, it is negligible with respect to the intrinsic spatial resolution. This is compatible with the expected precision of the survey measurements of ≈ 5 μm. This validation procedure was verified using Monte Carlo simulations of cosmic muons in the detector without misalignment, which give a spread in $\Delta x_{\rm loc}$ of about 25 μm, in agreement with that obtained from the data.

5.2 Track-to-point residuals in SSD

Another test that was performed uses two points in the outer SSD layer to define a straight track (no magnetic field) and inspects the residuals between points on the inner layer and the track. The residuals are calculated using the position along the track corresponding to the minimum of the weighted (dimensionless) distance to the point(2). Figure 10 shows

---

(2) The different expected resolutions in $r\varphi$ and z have been taken into account in the calculation of the

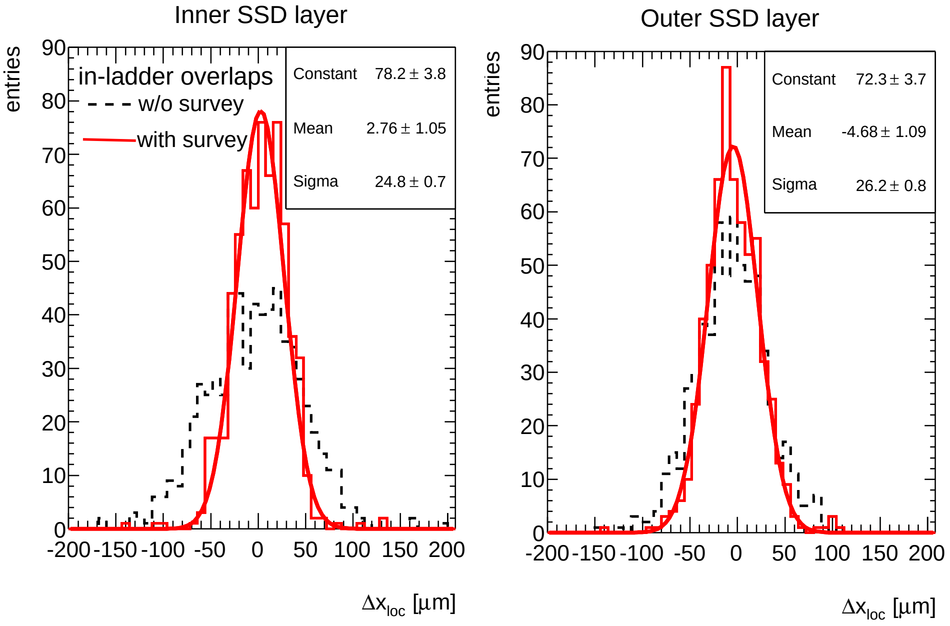

Figure 9: Distribution of $\Delta x_{\rm loc}$, the distance between two points in the module overlap regions along z on the same ladder, for the two layers of the SSD.

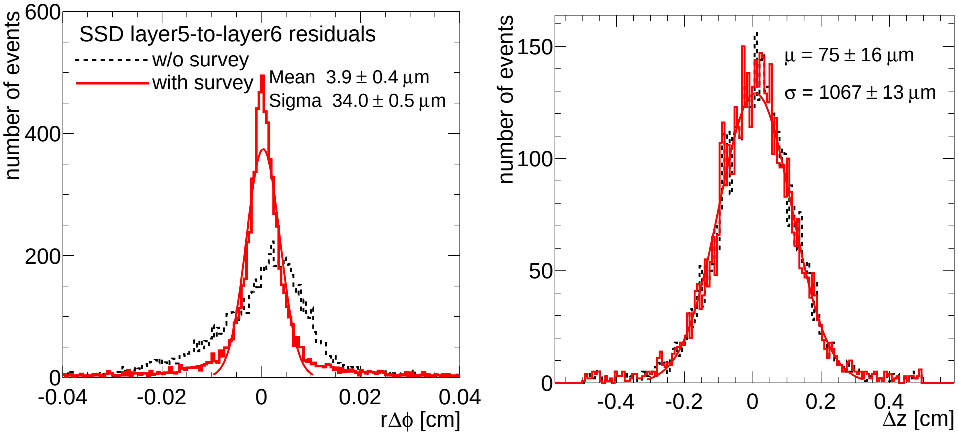

Figure 10: (colour online) Distribution of the $r\varphi$ (left panel) and z (right panel) residuals between tracks through layer 6 and points on layer 5. A gaussian fit truncated at $3\,\sigma$ (thin line) was used to determine the spread σ and mean μ.

the distribution of the $r\varphi$ (left-hand panel) and z residuals (right-hand panel) between tracks through layer 6 and points on layer 5. The width of the distributions is quantified by performing a gaussian fit truncated at $3\,\sigma$ (thin line in Fig. 10), giving $\sigma_{r\varphi} = 34\ \mu$m and $\sigma_z = 1067\ \mu$m. The spreads contain a contribution from the uncertainty in the track trajectory due to the uncertainties in the points on the outer layer. Assuming the same resolution on the outer and inner layer and taking into account the geometry of the detector, the effective single point resolution spread is $1/\sqrt{1.902}$ times the overall

---

distance of closest approach, by dividing the deviations by the expected uncertainties, i.e. making use of a dimensionless distance measure.

spread [17], so 25 μm and 778 μm in $r\varphi$ and z, respectively.

The effective resolution of the points in z is well within the expected uncertainty, indicating that no significant additional misalignment is present. For the $r\varphi$ direction, the obtained spread of 25 μm is larger than the intrinsic resolution of 20 μm. Multiple scattering of low-momentum tracks is expected to contribute to the broadening of the distribution, but no quantitative estimate of this effect was carried out. We can therefore not rule out that additional misalignments with an r.m.s. up to about 20 μm are present in the SSD. The mean residual is also non-zero, (3.9 ± 0.4) μm, which suggests that residual shifts at the 5–10 μm level could be present. These misalignments would have to be at the ladder level to be compatible with the result from the study with sensor module overlaps.

A third method that was used to verify the SSD survey consisted in performing tracking with pairs of points (2 points on layer 5 and two points on layer 6 or two sets of points on layer 5 and 6), and comparing the track parameters of both track segments. The conclusion from this method is consistent with the results from the track-to-point method. For details see [17].

6 ITS alignment with Millepede

In general, the task of track-based alignment algorithms is the determination of the set of geometry parameters that minimize the global χ^2 of the track-to-point residuals:

$$\chi^2_{\text{global}} = \sum_{\text{modules, tracks}} \vec{\delta}^{\,\text{T}}_{t,p}\,\mathbf{V}^{-1}_{t,p}\,\vec{\delta}_{t,p}\,. \tag{1}$$

In this expression, the sum runs over all the detector modules and all the tracks in a given dataset; $\vec{\delta}_{t,p} = \vec{r}_t - \vec{r}_p$ is the residual between the data point $\vec{r}_p$ and the reconstructed track extrapolation $\vec{r}_t$ to the module plane; $\mathbf{V}_{t,p}$ is the covariance matrix of the residual. Note that, in general, the reconstructed tracks themselves depend on the assumed geometry parameters. This section describes how this minimization problem is treated by Millepede [5, 18] —the main algorithm used for ITS alignment— and presents the first alignment results obtained with cosmic-ray data.

6.1 General principles of the Millepede algorithm

Millepede belongs to the *global least-squares minimization* type of algorithms, which aim at determining simultaneously all the parameters that minimize the global χ^2 in Eq. (1). It assumes that, for each of the local coordinates, the residual of a given track t to a specific measured point p can be represented in a linearized form as $\delta_{t,p} = \vec{a} \cdot \partial\delta_{t,p}/\partial\vec{a} + \vec{\alpha}_t \cdot \partial\delta_{t,p}/\partial\vec{\alpha}_t$, where $\vec{a}$ are the global parameters describing the alignment of the detector (three translations and three rotations per module) and $\vec{\alpha}_t$ are the local parameters of the track. The corresponding χ^2_{global} equation for n tracks with ν local parameters per track and for m modules with 6 global parameters ($N = 6\,m$ total global parameters) leads to a huge set of $N + \nu\,n$ normal equations. These can be written in the following partitioned matrix equation form:

$$\begin{pmatrix} \mathbf{C} & \mathbf{G}_1 & \dots & \dots & \mathbf{G}_n \\ \mathbf{G}_1^{\text{T}} & \mathbf{\Gamma}_1 & 0 & \dots & 0 \\ \vdots & \vdots & \vdots & \vdots & 0 \\ \mathbf{G}_n^{\text{T}} & 0 & \dots & 0 & \mathbf{\Gamma}_n \end{pmatrix} \begin{pmatrix} \vec{a} \\ \vec{\alpha}_1 \\ \vdots \\ \vec{\alpha}_n \end{pmatrix} = \begin{pmatrix} \vec{b} \\ \vec{\beta}_1 \\ \vdots \\ \vec{\beta}_n \end{pmatrix} \tag{2}$$

The sub-matrices $\mathbf{C}$ involve the derivatives of the residuals only over the global parameters (in the local frame of the sensor, where the covariance matrix is diagonal, $\mathrm{C}_{ij} = \sum_{t,p} \sigma_p^{-2} \partial\delta_{t,p}/\partial a_i \, \partial\delta_{t,p}/\partial a_j$), $\mathbf{\Gamma}_t$ depends only on the track t parameters ($\Gamma_{t,ij} = \sum_p \sigma_p^{-2} \partial\delta_{t,p}/\partial\alpha_{t,i} \, \partial\delta_{t,p}/\partial\alpha_{t,j}$) and $\mathbf{G}_t$ is for the local parameters of the track t and the global parameters ($\mathrm{G}_{t,ij} = \sum_p \sigma_p^{-2} \partial\delta_{t,p}/\partial a_i \, \partial\delta_{t,p}/\partial\alpha_{t,j}$). Similarly, the right-hand side of Eq. (2) is grouped to $b_i = \sum_{t,p} \sigma_p^{-2} \delta_{t,p} \, \partial\delta_{t,p}/\partial a_i$ and $\beta_{t,i} = \sum_p \sigma_p^{-2} \delta_{t,p} \, \partial\delta_{t,p}/\partial\alpha_{t,i}$.

The idea behind the Millepede method is to consider the local $\vec{\alpha}$ parameters as nuisance parameters that are eliminated using the Banachiewicz identity [19] for partitioned matrices:

$$\left(\begin{array}{c|c} \mathbf{C}_{11} & \mathbf{C}_{12} \\ \hline \mathbf{C}_{12} & \mathbf{C}_{22} \end{array} \right)^{-1} = \left(\begin{array}{c|c} \mathbf{B} & -\mathbf{B}\mathbf{C}_{12}\mathbf{C}_{22}^{-1} \\ \hline -\mathbf{C}_{22}^{-1}\mathbf{C}_{12}^{\mathrm{T}}\mathbf{B} & \mathbf{C}_{22}^{-1} + \mathbf{C}_{22}^{-1}\mathbf{C}_{12}^{\mathrm{T}}\mathbf{B}\mathbf{C}_{12}\mathbf{C}_{22}^{-1} \end{array} \right) \tag{3}$$

with $\mathbf{B} = \left(\mathbf{C}_{11} - \mathbf{C}_{12}\mathbf{C}_{22}^{2}\mathbf{C}_{12}^{\mathrm{T}}\right)^{-1}$. In fact, the full matrix of all the $N+\nu n$ parameters is not built explicitly: using Eq. (3) the set of N normal equations for the global parameters is constructed by subtracting from $\mathbf{C}$ and $\vec{b}$ the contributions related to the local parameters. If needed, linear constraints on the global parameters can be added using the Lagrange multipliers. Historically, two versions, Millepede and Millepede II, were released. The first one, written in Fortran, was performing the calculation of the residuals, the derivatives and the final matrix elements as well as the extraction of the exact solution in one single step, keeping all necessary information in computer memory. The large memory and CPU time needed to extract the exact solution of a $N \times N$ matrix equation effectively limited its use to $N < 10,000$ global (alignment) parameters. This limitation was removed in the second version, Millepede II. Software-wise the algorithm is split in two parts: the first one (available in C and Fortran) stores in an intermediate file the residuals, derivatives and constraints provided by the user, while the second one (in Fortran) processes these data, builds the necessary matrices (optionally in sparse format, to save memory space) and solves them using advanced iterative methods, much faster than the exact methods.

6.2 Millepede for the ALICE ITS

Following the development of Millepede, ALICE had its own implementation of both versions, hereafter indicated as MP and MPII, within the AliRoot framework [6]. Both consist of a detector independent solver class, responsible for building and solving the matrix equations, and a class interfacing the former to specific detectors[3)]. While MP closely follows the original algorithm [5], MPII has a number of extensions. In addition to the MinRes matrix equation solution algorithm offered by the original Millepede II, the more general FGMRES [21] method was added, as well as the powerful ILU(k) matrix preconditioners [22]. All the results shown in this work are obtained with MPII.

The track-to-point residuals, used to construct the global χ^2, are calculated using a parametric straight line $\vec{r}(t) = \vec{a} + \vec{b}\,t$ or helix $\vec{r}(t) = \{a_x + r\cos(t+\varphi_0), a_y + r\sin(t+\varphi_0), a_z + b_z\,t\}$ track model, depending on the presence of the magnetic field. The full error matrix of the measured points is accounted for in the track fit, while multiple scattering is ignored, since it has no systematic effect on the residuals.

Special attention was paid to the possibility to account for the complex hierarchy of the alignable volumes of the ITS, shown in Fig. 2, in general leading to better description

---

[3)] MP was originally implemented for the Muon Arm alignment and has been later interfaced to ITS, while MPII is currently interfaced to ITS only.

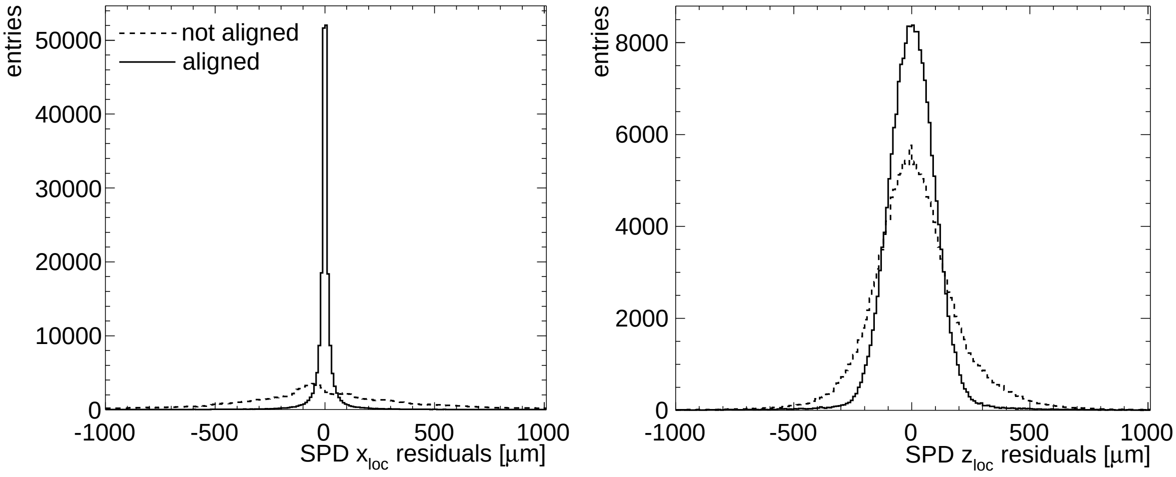

Figure 11: Example of Millepede residuals in the local reference frame of the SPD modules before and after the alignment.

of the material budget distribution after alignment. This is achieved by defining explicit parent–daughter relationships between the volumes corresponding to mechanical degrees of freedom in the ITS. The alignment is performed simultaneously for the volumes on all levels of the hierarchy, e.g. for the SPD the corrections are obtained in a single step for the sectors, the half-staves within the sectors and the modules within the half-staves. Obviously, this leads to a degeneracy of the possible solutions, which should be removed by an appropriate set of constraints. We implemented the possibility to constrain either the mean or the median of the corrections for the daughter volumes of any parent volume. While the former can be applied via Lagrange multipliers directly at the minimization stage, the latter, being non-analytical, is applied a posteriori in a dedicated afterburner. The relative movement δ of volumes for which the survey data is available (e.g. SDD and SSD modules) can be restricted to be within the declared survey precision σ_{survey} by adding a set of gaussian constraints $\delta^2/\sigma^2_{\mathrm{survey}}$ to the global χ^2.

We report here a few example figures to illustrate the bare output results from Millepede II for the alignment of the SPD detector (in this case), while the analysis of the alignment quality will be presented in the next section. Figure 11 shows an example of the residuals in SPD (in the local reference frame of the modules) before and after alignment. Figure 12 (left) shows an example of the corrections obtained for the z coordinate of the alignable volumes in SPD: the corrections are distributed among the different levels of hierarchy (sectors, half-staves, modules). For comparison, the cross markers show the result of the non-hierarchical alignment —modules only (smallest alignable volumes) are aligned. Figure 12 (right) shows, instead, the obtained corrections for the φ_{loc} angle (rotation of the volume with respect to its z_{loc} axis), indicating that the largest misalignments are at the level of the half-staves with respect to the carbon fiber support sectors.

6.3 Results on alignment quality

The SPD detector was first aligned using about 5×10^4 cosmic-ray tracks, with two points in the inner layer and two points in the outer layer, collected in 2008 with the magnetic field switched off. As described in the previous section, the hierarchical alignment procedure consisted in (cfr. Fig. 2): aligning the ten sectors with respect to each other, the twelve

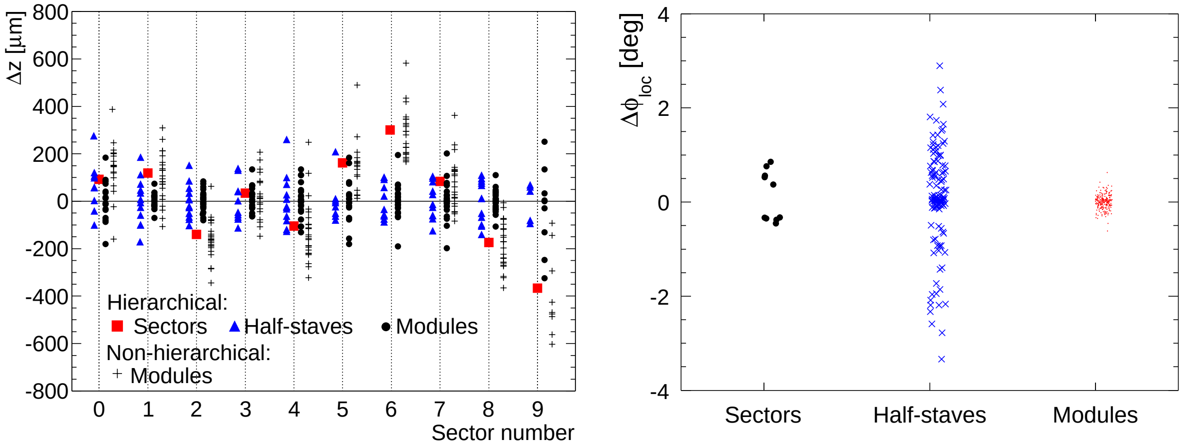

Figure 12: (colour online) Example of hierarchical SPD alignment. Left: corrections for the z coordinate of the SPD volumes as a function of the sector number. Crosses: results from the alignment with all misalignments attributed to the module degrees of freedom. Hierarchical alignment resolves the corrections in contributions from sectors (squares), half-staves (triangles) and module (circles) misalignments. Right: corrections to the $\varphi_{\rm loc}$ angle obtained in the hierarchical alignment.

half-staves of each sector with respect to the sector, and the two modules of each half-stave with respect to the half-stave.

Mainly, the following two observables are used to check the quality of the obtained alignment: the top half-track to bottom half-track matching at the plane $y = 0$, and the track-to-point distance for the "extra" points in the acceptance overlaps.

For the first observable, the cosmic-ray track is split into the two track segments that cross the upper ($y > 0$) and lower ($y < 0$) halves of the ITS barrel, and the parameters of the two segments are compared at $y = 0$. The main variable is $\Delta xy|_{y=0}$, the track-to-track distance at $y = 0$ in the (x, y) plane transverse to beam-line. This observable, that is accessible only with cosmic-ray tracks, provides a direct measurement of the resolution on the track transverse impact parameter d_0; namely: $\sigma_{\Delta xy|_{y=0}}(p_{\rm t}) = \sqrt{2}\,\sigma_{d_0}(p_{\rm t})$. Since the data used for the current analysis were collected without magnetic field, they do not allow us to directly assess the d_0 resolution (this will be the subject of a future work). However, also without a momentum measurement, $\Delta xy|_{y=0}$ is a powerful indicator of the alignment quality, as we show in the following.

Figure 13 (left) shows the the distribution of $\Delta xy|_{y=0}$ at the various levels of the hierarchical SPD alignment, from the uncorrected data to the final step with the corrections for sectors, half-staves and modules applied. The two track segments are required to have a point in each of the SPD layers and to pass, in the transverse plane, within 1 cm from the origin (this cut selects tracks with a similar topology as those produced in collisions and, in particular, rejects tracks that have small incidence angles on the inner layer modules). The figure indicates that the main alignment improvement is obtained when applying the corrections at the level of the half-staves, which are the largest, as shown by Fig. 12 (right). A gaussian fit to the final distribution in the range $[-100\ \mu\text{m}, +100\ \mu\text{m}]$, shown in Fig. 13 (right), gives a centroid compatible with zero and a spread $\sigma \approx 50\ \mu$m. For comparison, a spread of 38 μm is obtained from a Monte Carlo simulation, with the ideal geometry of the ITS (without misalignment), of comic-muons generated according

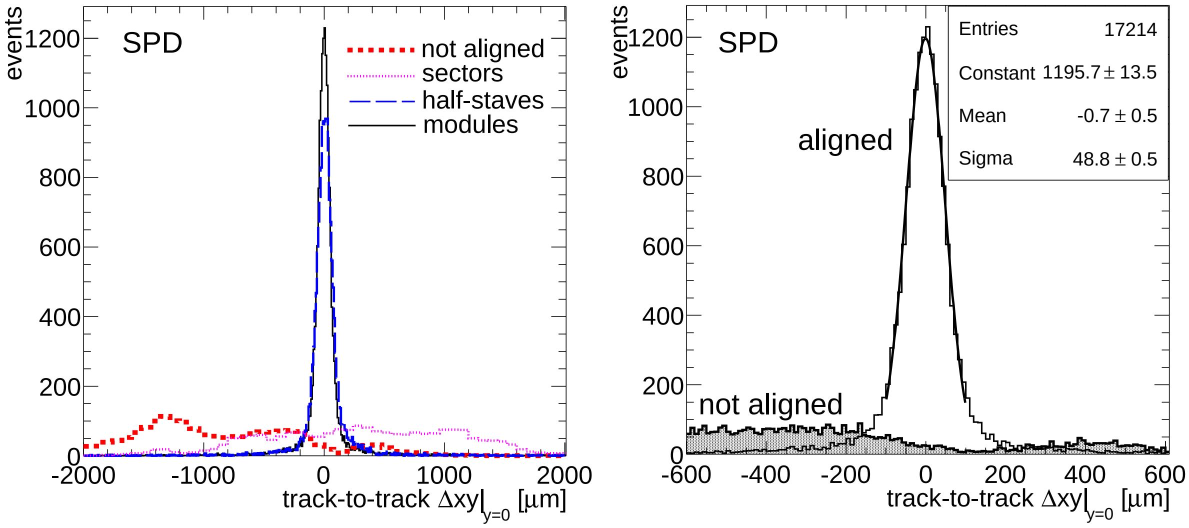

Figure 13: (colour online) Left: distribution of $\Delta xy|_{y=0}$ for SPD as obtained applying the corrections up to a given hierarchical level. Right: fit of the $\Delta xy|_{y=0}$ distribution with all corrections applied.

to the momentum spectrum measured by the ALICE TPC in cosmic runs with magnetic field. When only the SPD detector is used and the tracks are straight lines (no magnetic field), the spread of the $\Delta xy|_{y=0}$ distribution can be related in a simple way to the effective spatial resolution $\sigma_{\rm spatial}$, inclusive of the intrinsic sensor resolution and of the residual misalignment. For tracks passing close to the beam line (as in our case, with the cut at 1 cm), we have:

$$\sigma^2_{\Delta xy|_{y=0}} \approx 2\,\frac{(r^2_{\rm SPD1}\sigma^2_{\rm spatial,SPD1} + r^2_{\rm SPD2}\sigma^2_{\rm spatial,SPD2})}{(r_{\rm SPD1} - r_{\rm SPD2})^2} \approx 2\,\frac{r^2_{\rm SPD1} + r^2_{\rm SPD2}}{(r_{\rm SPD1} - r_{\rm SPD2})^2}\,\sigma^2_{\rm spatial}\,, \quad (4)$$

where the inner and outer SPD layers are indicated as SPD1 and SPD2, respectively. This relation neglects the effect of multiple scattering in the pixels and in the beam pipe, which is certainly one of the reasons why the $\Delta xy|_{y=0}$ distribution is not gaussian outside the central region, most likely populated by the high-momentum component of the cosmic muons. Using the fit result, $\sigma_{\Delta xy|_{y=0}} \approx 50$ μm, obtained in the central region $[-100\ \mu{\rm m}, +100\ \mu{\rm m}]$, we estimate the value $\sigma_{\rm spatial} \approx 14$ μm, not far from the intrinsic resolution of about 11 μm extracted from the simulation. However, a precise estimation of the effective spatial resolution with this method requires the measurement of the track momentum, to account properly for the multiple scattering contribution. The statistics collected in 2008 with magnetic field did not allow a momentum-differential analysis.

The next step in the alignment procedure is the inclusion of the SSD detector. As shown in section 5, the survey measurements already provide a very precise alignment, with residual misalignment levels of the order of less than 5 μm for modules on the ladder and of about 20 μm for ladders. Because of the limited available statistics ($\approx 2\times10^4$ tracks with four points in SPD and four points in SSD), the expected level of alignment obtained with Millepede on single SSD modules is significantly worse than the level reached with the survey measurements. For this reason, Millepede was used only to align the whole SPD barrel with respect to the SSD barrel and to optimize the positioning of large sets of SSD modules, namely the upper and lower halves of layers 5 and 6. For this last step, the

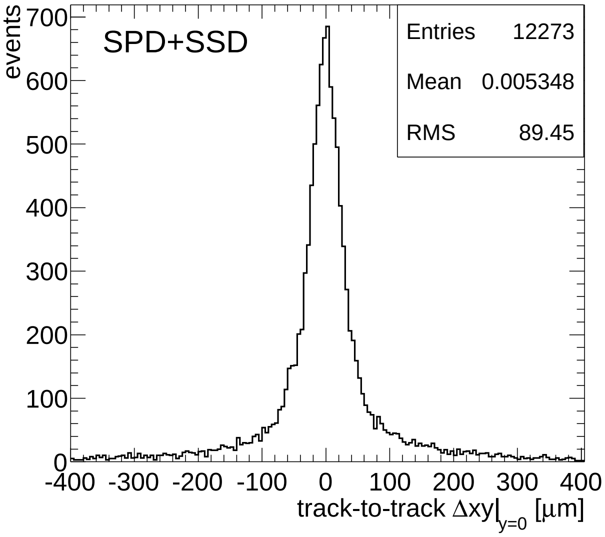

Figure 14: Distribution of the distance in the transverse plane ($\Delta xy|_{y=0}$) for track segments reconstructed in the upper and lower parts of SPD+SSD layers. Each track segment is requested to have four assigned points. SSD survey and Millepede alignment corrections are applied.

improvement on the global positioning of the SSD layers was verified by comparing the position and direction of the pairs of SSD-only track segments built using: two points in the upper and two in the lower half-barrel (upper–lower configuration) or two points the inner and two in the outer layer (inner–outer configuration). As reported in Table 2, all mean values are compatible with zero after the alignment. Figure 14 shows the distribution of $\Delta xy|_{y=0}$ for pairs of track segments, each reconstructed with two points in SPD and two in SSD, i.e. the merged cosmic-ray track has eight points in SPD+SSD. It can be seen that, when the SSD survey and the Millepede alignment are applied, the distribution is centred at zero and very narrow (FWHM ≈ 60 μm), but it shows non-gaussian tails, most likely due to multiple scattering. A more precise alignment of the SSD using high-momentum tracks will be performed with the 2009 cosmic-ray and proton–proton data.

The second alignment quality observable is the Δx_{loc} distance between points in the region where there is an acceptance overlap between two modules of the same layer. Because of the short radial distance between the two overlapping modules (a few mm), the effect of multiple scattering is negligible. However, in order to relate the spread of

Table 2: Mean values of the distributions of the linear ($\Delta xy|_{y=0}$) and angular ($\Delta\varphi|_{y=0}$) SSD track-to-track distances in the transverse plane for the upper–lower and inner–outer configurations, before and after Millepede alignment. The survey corrections are always applied.

Configuration	Variable	Mean before alignment	Mean after alignment
upper–lower	$\Delta xy\|_{y=0}$ [μm]	120±7	-5±6
upper–lower	$\Delta\varphi\|_{y=0}$ [mdeg]	4±1	-1±1
inner–outer	$\Delta xy\|_{y=0}$ [μm]	-1.8±0.6	0.5±0.6
inner–outer	$\Delta\varphi\|_{y=0}$ [mdeg]	-1±0.1	0.0±0.1

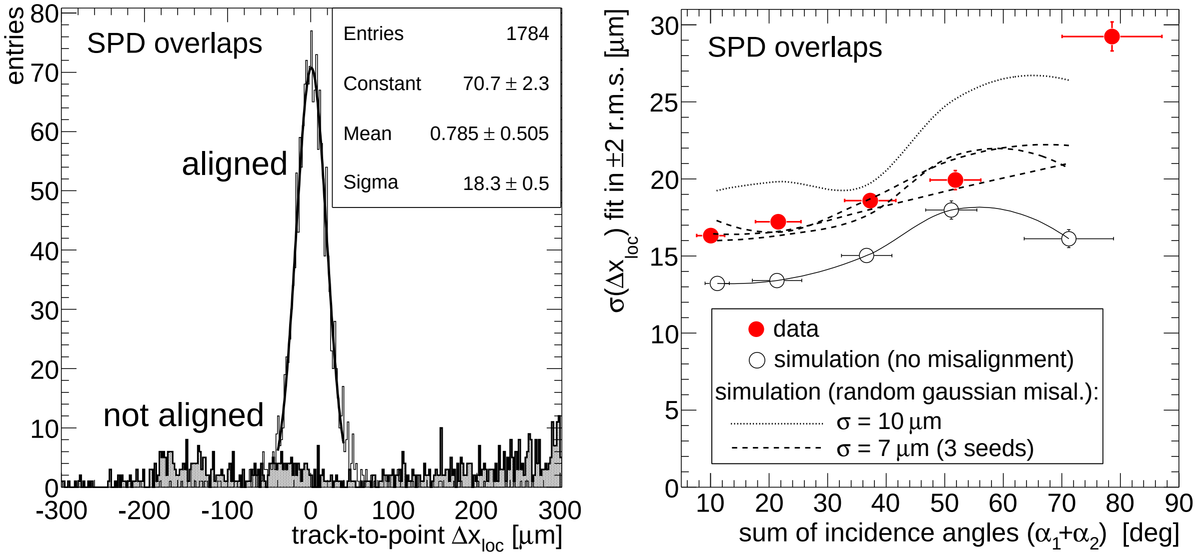

Figure 15: (colour online) SPD double points in acceptance overlaps. Left: track-to-point $\Delta x_{\rm loc}$ for "extra" points before and after alignment. Right: σ of the $\Delta x_{\rm loc}$ distributions as a function of the track-to-module incidence angle selection; 2008 cosmic-ray data are compared to the simulation with different levels of residual misalignment. See text for details.

$\Delta x_{\rm loc}$ to the effective resolution, the dependence of the intrinsic sensor resolution on the track-to-module incidence angle has to be accounted for. In particular, for SPD, due to the geometrical layout of the detector (Fig. 3, left), the track-to-module incidence angles in the transverse plane are in general not equal to 90° and they are very different for two adjacent overlapping modules crossed by the same track. If $\Delta x_{\rm loc}$ is defined as described in section 5, the error on $\Delta x_{\rm loc}$ can be related to the effective spatial resolution of the two points, $\sigma_{\rm spatial}$, as:

$$\sigma^2_{\Delta x_{\rm loc}} = \sigma^2_{\rm spatial}(\alpha_2) + \sigma^2_{\rm spatial}(\alpha_1)\cos^2(\varphi_{12}) \tag{5}$$

where the 1 and 2 subscripts indicate the two overlapping points, α_i is the incidence angle of the track on the module plane, and φ_{12} is the relative angle between the two module planes, which is 18° and 9° on the inner and outer SPD layer, respectively. Note that, for SSD overlaps on the same ladder, we have $\alpha_1 = \alpha_2 \simeq 90°$ and $\varphi_{12} = 0$; therefore, $\sigma_{\Delta x_{\rm loc}} = \sqrt{2}\,\sigma_{\rm spatial}$, which is the relation we used in section 5.

We start by showing, in Fig. 15 (left), the track-to-point distance $\Delta x_{\rm loc}$ for the SPD "extra" points in the transverse plane, before and after the Millepede alignment. The extra points are not used in the alignment procedure. The spread of the distribution is $\sigma \approx 18\ \mu$m, to be compared to $\sigma \approx 15\ \mu$m from a Monte Carlo simulation with ideal geometry. An analysis of the $\Delta x_{\rm loc}$ distance as a function of the α incidence angle has been performed: five windows on the sum $(\alpha_1 + \alpha_2)$ of the incidence angles on the two overlapping modules have been considered. These cuts sample increasing ranges of incidence angles from 0° to 50°. Figure 15 (right) shows the spread of the $\Delta x_{\rm loc}$ distribution for the different incidence angle selections: a clear dependence of the spread (hence of the spatial resolution) on the incidence angle can be seen. This dependence was already observed in SPD test-beam measurements [23, 24], which were used to tune the detector response simulation in the AliRoot software. In the same figure, Monte Carlo simulation

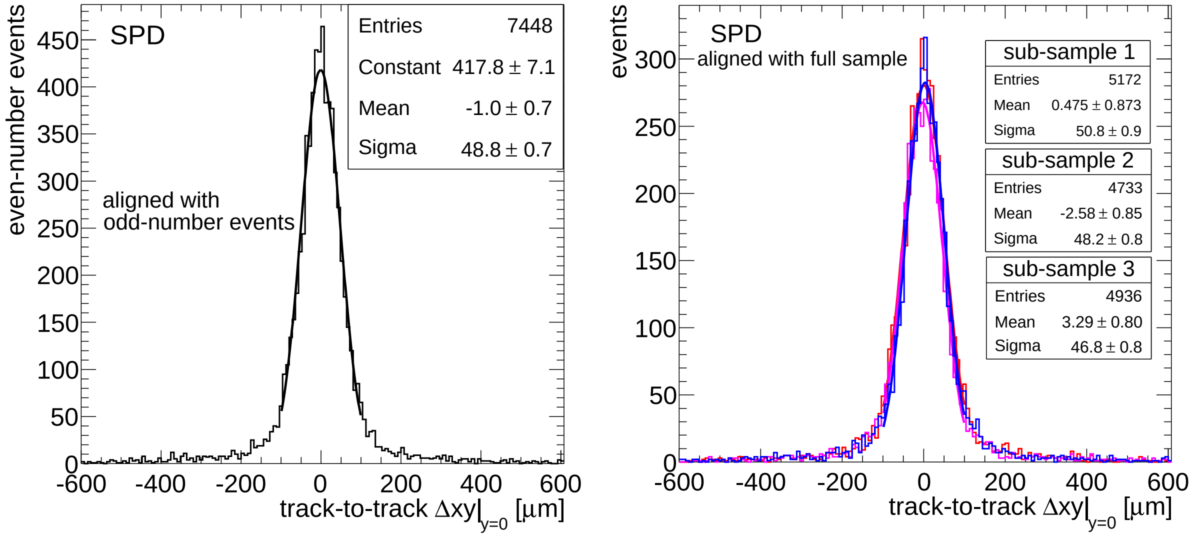

Figure 16: (colour online) SPD alignment stability tests. Left: distribution of the $\Delta xy|_{y=0}$ distance obtained when aligning with every second track and checking the alignment with the other tracks. Right: $\Delta xy|_{y=0}$ distribution for three successive subsamples collected in 2008 (July, August, September-October).

results are reported for comparison: simulation with ideal geometry (open circles) and with a misaligned geometry obtained using a random gaussian residual misalignment (dashed lines: misalignments with $\sigma = 7$ μm and three different seeds; dotted line: misalignments with $\sigma = 10$ μm). The 2008 data are well described by the simulation with a random residual misalignment with $\sigma \approx 7$ μm. However, this conclusion is based on the assumption that the intrinsic resolution is the same in the real detector and in the simulation. Since the intrinsic resolution can slightly vary depending on the working conditions of the detector (e.g. the settings used for the bias voltage and for the threshold), the value of 7 μm for the residual misalignment should be taken only as an indication. Furthermore, this is an equivalent random misalignment, while the real misalignments are likely non-gaussian and to some extent correlated among different modules.

We also studied the robustness and the stability of the obtained results. First, we divided the data sample in two parts and used every second track to align the SPD and the others to check the alignment quality. The corresponding $\Delta xy|_{y=0}$ distribution is presented in the left-hand panel of Fig. 16: the distribution is centred at zero and has the same $\sigma \approx 50$ μm as in the case of aligning with all tracks. In the right-hand panel of the same figure, Fig. 16, we address the stability in time of the alignment results by plotting the $\Delta xy|_{y=0}$ distribution for three subsamples roughly corresponding to July 08, August 08, and September-October 08. The full statistics was used to obtain the alignment. The alignment quality was stable in time during the whole 2008 run.

Finally, we used the data with the 0.5 T magnetic field switched on (a few thousand events collected at the end of the 2008 cosmic run) to perform dedicated checks to evaluate a possible effect of the field on the alignment. We applied the alignment correction extracted from data with B = 0 to data with B = ± 0.5 T. In the left-hand panel of Fig. 17 we report the track-to-point distance for extra points in SPD acceptance overlaps for B = 0, +0.5 T and -0.5 T data. The fitted widths of the distributions with field on and field off (Fig. 15, left) are compatible. We also checked the track-to-point residuals,

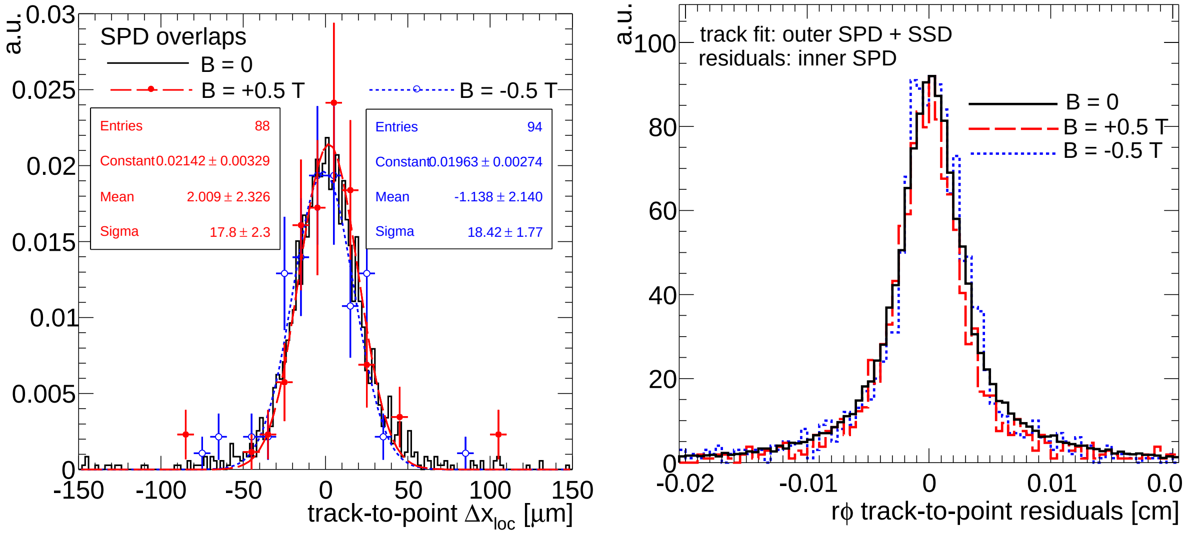

Figure 17: (colour online) Alignment validation checks with magnetic field switched on. Left: track-to-point distance for extra points in SPD acceptance overlaps. Right: track-to-point residuals in the inner SPD layer (track fit in outer SPD layer and in the two SSD layers). In both panels the three histograms are normalized to the same integral.

calculated by fitting the tracks in the SSD layers and the outer SPD layer and evaluating the residuals in the inner SPD layer. In Fig. 17 (right) the comparison between the residuals without magnetic field, with $+0.5$ T and with -0.5 T is shown. Also in this case, the distributions without field and with the two field polarities are compatible.

6.4 Prospects for inclusion of SDD in the Millepede procedure

The alignment of the SDD detectors for the $x_{\rm loc}$ coordinate (reconstructed from the drift time) is complicated by the interplay between the geometrical misalignment and the calibration of drift speed and t_0 (defined in section 2.2). The t_0 parameter accounts for the delays between the time when a particle crosses the detector and the time when the front-end chips receive the trigger signal. Two methods have been developed in order to obtain a first estimate of the t_0 parameter. The first, and simpler, method consists in extracting the t_0 from the minimum measured drift time on a large statistics of reconstructed SDD points. In practice, the distribution of measured drift times is built and the sharp rising part of the distribution at small drift times is fitted with an error function. The t_0 value is then calculated from the fit parameters. The second method measures the t_0 from the distributions of residuals along the drift direction ($x_{\rm loc}$) between tracks fitted in SPD and SSD layers and the corresponding points reconstructed in the SDD. These distributions, in case of mis-calibrated t_0, show two opposite-signed peaks corresponding to the two separated drift regions of each SDD module, where electrons move in opposite directions (see Fig. 4, right). The t_0 can be calculated from the distance of the two peaks and the drift speed. This second procedure has the advantage of requiring smaller statistics, because it profits from all the reconstructed tracks, with the drawback of relying on SDD calibration parameters (the drift speed and possibly the correction maps). Moreover, being based on track reconstruction, it might be biased by SPD and/or SSD misalignments.

Depending on the available statistics, the t_0 determination with these two methods can be done at the level of SDD barrel, SDD ladders or SDD modules. The t_0 parameter

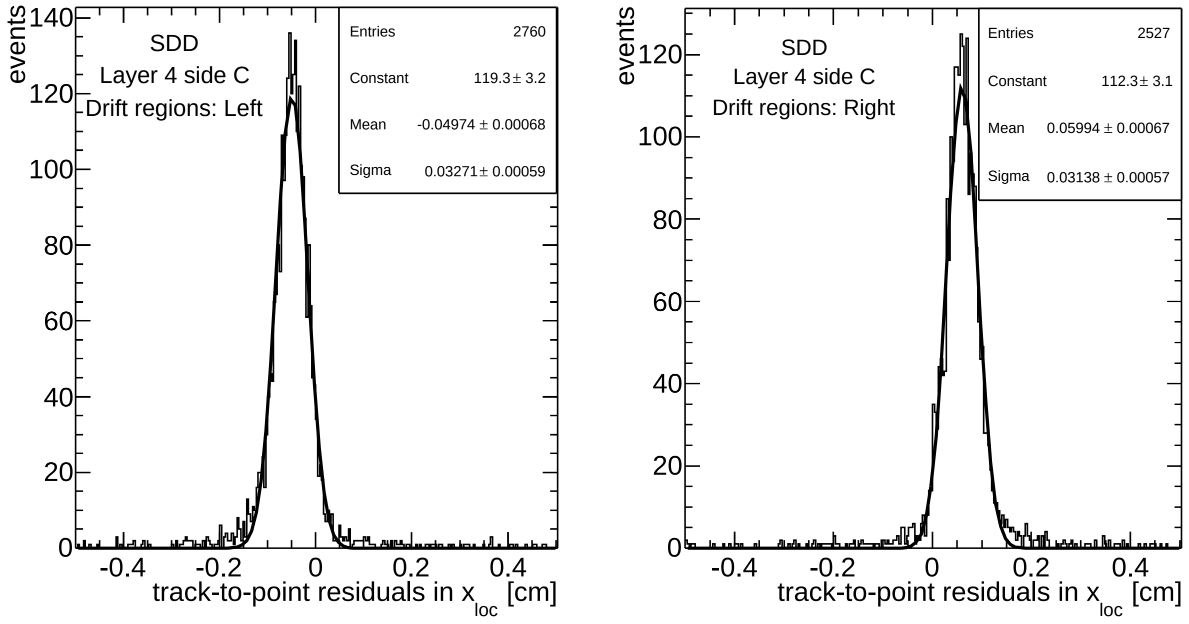

Figure 18: Distribution of track-to-point residuals in the two drift regions for the SDD modules of layer 4 side C ($z < 0$). Tracks are fitted using only their associated points in SPD and SSD. The Millepede alignment corrections for SPD and SSD are included, as well as the SSD survey.

needs actually to be calibrated individually for each of the 260 SDD modules, because of differences in the overall length of the cables connecting the DAQ cards and the front-end electronics. In particular, a significant difference is expected between modules of the A ($z > 0$) and C sides ($z < 0$), due to the ≈6 m difference in the length of the optical fibres connecting the ITS ladders to the DAQ cards. With the first 2000 tracks, it is possible to determine the t_0 from track-to-point residuals for 4 sub-samples of modules, i.e. separating sensors connected to sides A and C of layers 3 and 4. An example of residual distributions for the left and right drift sides of the modules of layer 4 side C is shown in Fig. 18. The Millepede alignment corrections for SPD and SSD are applied in this case, and it has been checked that, if they are not applied, the centroid positions in this figure are not affected significantly, while the spread of the distributions increases, as it could be expected. A difference of ≈35 ns between sides A and C of each SDD layer has been observed, in agreement with the ≈6 m difference in fibre lengths (the propagation time of light in optical fibres is 4.89 ns/m). With larger statistics (≈ 35,000 tracks), it is possible to extract the t_0 for each half-ladder, which requires building 36(ladders)×2(A/C sides) pairs of histograms like the ones shown in Fig. 18. Since the spread on optical fibres length among half-ladders connected to the same (A or C) side is ≈ 1.5 m, the effect on the half-ladder t_0 is expected to be below 7 ns. This fact, however, could not be verified with the cosmic data collected in 2008, because only few ladders (the ones close to the vertical) were illuminated enough to allow the t_0 determination. A systematic difference on the t_0 is finally expected among modules connected to the same ladder, due to the different length of the cables connecting the front-end chips with the electronic boards located at the end of the ladder. The maximal difference amounts to ≈ 15 cm on layer 3 and 22 on layer 4, corresponding to less than 1 ns effect on t_0. It should be noted that

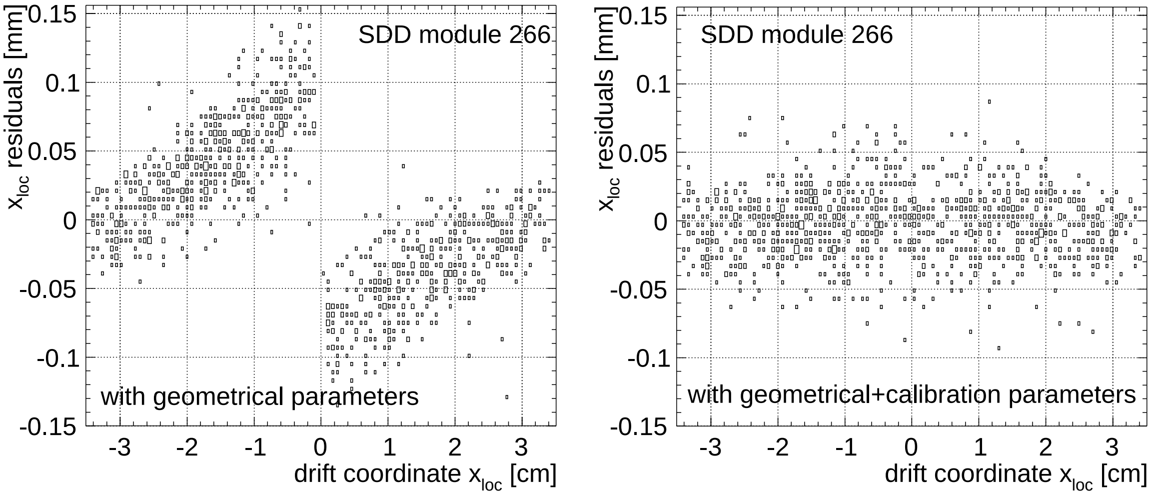

Figure 19: Residuals along the drift coordinate for one SDD module as a function of drift coordinate after Millepede alignment with only geometrical parameters (left) and with geometrical+calibration parameters (right).

given the ≈ 6.5 μm/ns of drift speed, a bias of 1 ns on the t_0 can lead to a significant effect on the reconstructed position along the drift coordinate $x_{\rm loc}$.

After a first calibration with these methods, a refinement of the t_0 determination is obtained by running the Millepede minimization with the t_0 as a free global parameter for each of the 260 SDD modules. Similarly, the drift speed is considered as a free parameter for those SDD modules with mal-functioning injectors. This allows to assess at the same time geometrical alignment and calibration parameters of the SDD detectors. An example is shown for a specific SDD module in Fig. 19, where the $x_{\rm loc}$ residuals along the drift direction are shown as a function of $x_{\rm loc}$. In the left-hand panel, the result obtained using only the geometrical rotations and translations as free parameters in the Millepede minimization is shown. The clear systematic shift between the two drift regions ($x_{\rm loc} < 0$ and $x_{\rm loc} > 0$) is due to both mis-calibrated t_0 and biased drift speed (this is a module with non-working injectors). These systematic effects are no longer present when also the calibration parameters are fitted by Millepede (right-hand panel). It should be pointed out that the width of the SDD residual distributions shown in Figs. 18 and 19 does not correspond to the expected resolution on SDD points along drift coordinate because of the jitter between the time when the muon crosses the detectors and the asynchronous SPD FastOR trigger, which has an integration time of 100 ns.

7 SPD alignment with an iterative local method

We developed an alignment method that performs a (local) minimization for each single module and accounts for correlations between modules by iterating the procedure until convergence is reached. A similar approach is considered by both the CMS and ATLAS experiments [25, 26, 27]. The main difference between this method and the Millepede algorithm is that only in the latter the correlations between the alignment parameters of all modules are explicitly taken into account. Conversely, the local module-by-module algorithm assumes that the misalignments of the modules crossed by a given track are uncorrelated and performs the minimization of the residuals independently for each mod-

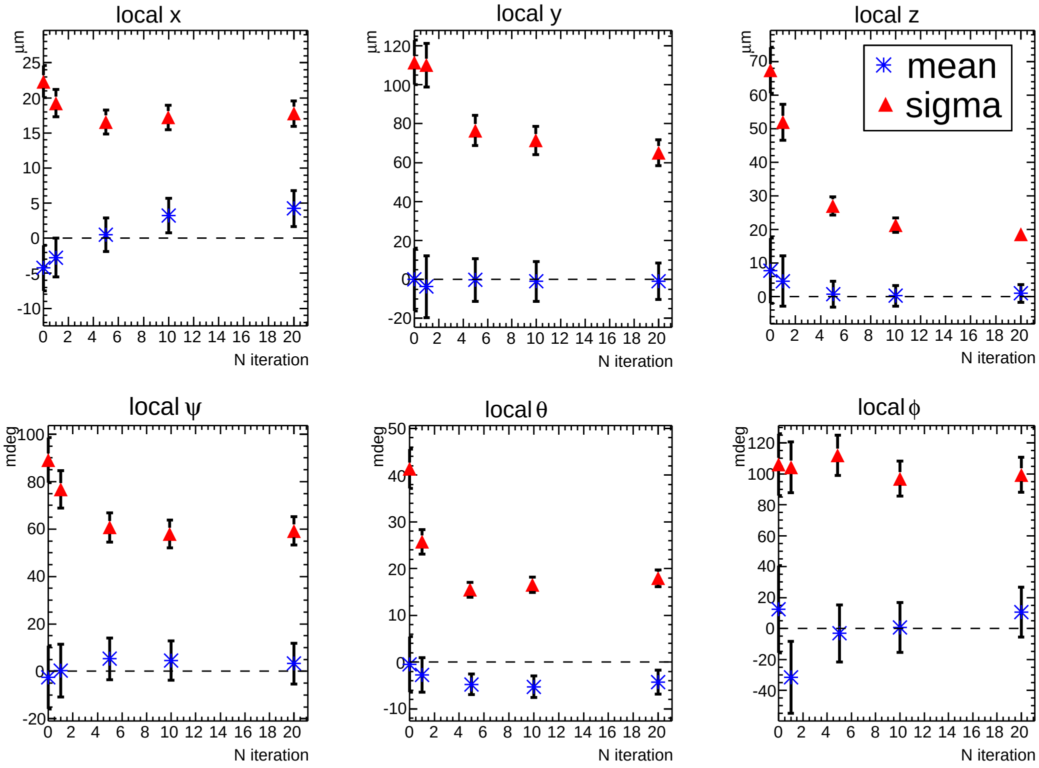

Figure 20: Example of the convergence of the iterative method for SPD on simulated cosmic-muon events (see text for details). The mean (star markers) and r.m.s. (triangle markers) of the distribution of the residuals, for all SPD modules, between the true and estimated value of the six local alignment parameters (three translations in the upper row and three rotations in the lower row) are shown.

ule. The comparison of the alignment parameters from this method and from Millepede would allow us to have a further validation of the results achieved with the latter.

In the local method we minimize, module-by-module, the following local χ^2 function of the alignment parameters of a single module:

$$\begin{aligned} \chi^2_{\text{local}}(\vec{a}_{\text{tra}}, \mathbf{A}_{\text{rot}}) &= \sum_{\text{tracks}} \vec{\delta}^{\,\text{T}}_{t,p}\, \mathbf{V}^{-1}_{t,p}\, \vec{\delta}_{t,p} \\ &= \sum_{\text{tracks}} \left(\vec{r}_t - \mathbf{A}_{\text{rot}}\vec{r}_p - \vec{a}_{\text{tra}}\right)^{\text{T}} \left(\mathbf{V}_t + \mathbf{V}_p\right)^{-1} \left(\vec{r}_t - \mathbf{A}_{\text{rot}}\vec{r}_p - \vec{a}_{\text{tra}}\right) . \quad (6) \end{aligned}$$

Here, the sum runs over the tracks passing through the module, $\vec{r}_p$ is the position of the measured point on the module while $\vec{r}_t$ is the crossing point on the module plane of the track t fitted with all points but $\vec{r}_p$. $\mathbf{V}_t$ and $\mathbf{V}_p$ are the covariance matrices of the crossing point and of the measured point, respectively. The six alignment parameters enter this formula in the vector $\vec{a}_{\text{tra}}$, the alignment correction for the position of the centre of the module, and in the rotation matrix $\mathbf{A}_{\text{rot}}$, the alignment correction for the orientation of the plane of the module. The alignment correction is supposed to be small so that the rotation matrix can be approximated as the unity matrix plus a matrix linear in the angles. In this way, the χ^2_{local} is a quadratic expression of the alignment parameters and the minimization can be performed by simple inversion. The χ^2_{local} function in Eq. (6) can be written in the same way also for a set of modules considered as a rigid block. The track

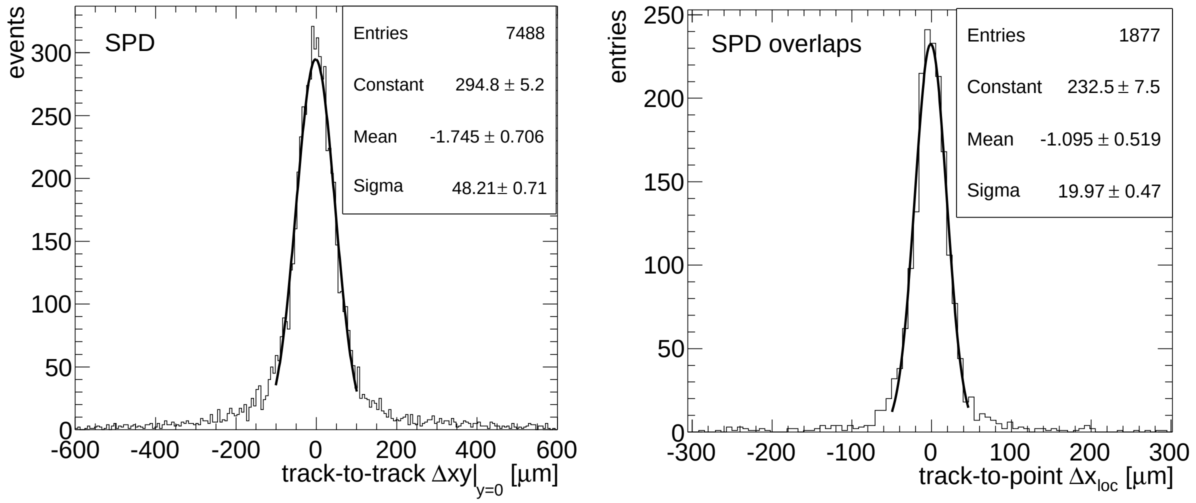

Figure 21: SPD alignment quality results for the iterative local method. Left: track-to-track $\Delta xy|_{y=0}$ distribution defined in section 6.3, using only SPD points. Right: track-to-point $\Delta x_{\rm loc}$ distribution for extra points in acceptance overlaps.

parameters are not affected by the misalignment of the module under study, because the point is not used in the fit, while the positions of the crossing points are affected, because the tracks are propagated to the plane of the module defined in the ideal geometry. This is taken into account by adding a large error along the track direction to the covariance matrix of the crossing point.

Given that this is a local method, it is expected to work at best if two conditions are fulfilled: the correlation between the misalignments of different modules is small and the tracks used to align a given module cross several other modules. In order to limit the bias that can be introduced by modules with low statistics, for which the second condition is normally not met, we align the modules following a sequence of decreasing number of points. To reduce the residual correlation between the alignment parameters obtained for the different modules, we iterate the procedure until the parameters converge. We checked the performance of the algorithm using a simulation of about 10^5 cosmic-muon events, generated with randomly distributed misalignments with local translations in a range of ± 100 μm, and local rotations that give equivalent mean shifts. In Fig. 20 the r.m.s. and the mean of the distributions of the differences between the SPD input parameters and the recovered values are shown as a function of the number of iterations. The convergence is reached after about 10 iterations.

For the ITS alignment using the 2008 cosmic-ray data, we aligned only the SPD modules using this method. Like for Millepede, we adopted a hierarchical approach. Given the excellent precision of the SSD survey measurements, we used these two layers as a reference. We aligned as a first step the whole SPD barrel with respect to the SSD, then the two half-barrels with respect to the SSD, then the SPD sectors with respect to the SSD. In the last step, we used SPD and SSD points to fit the tracks and we aligned the individual sensor modules of the SPD. Figure 21 shows the top–bottom track-to-track $\Delta xy|_{y=0}$ distribution obtained using only the SPD points (left-hand panel) and the track-to-point $\Delta x_{\rm loc}$ for the double points in acceptance overlaps (right-hand panel), after alignment. Both distributions are compatible (mean and sigma from a gaussian fit) with the corresponding distributions after Millepede alignment. We thus conclude that the

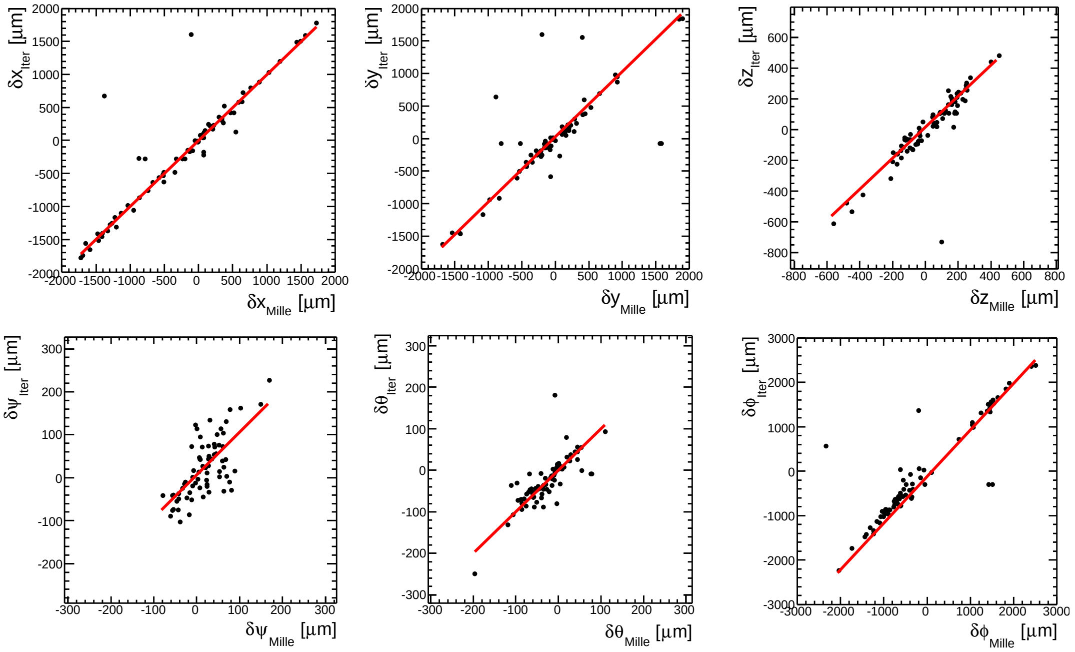

Figure 22: Correlation between the alignment parameters obtained from Millepede (horizontal axis) and the iterative method (vertical axis), for the inner SPD layer modules.

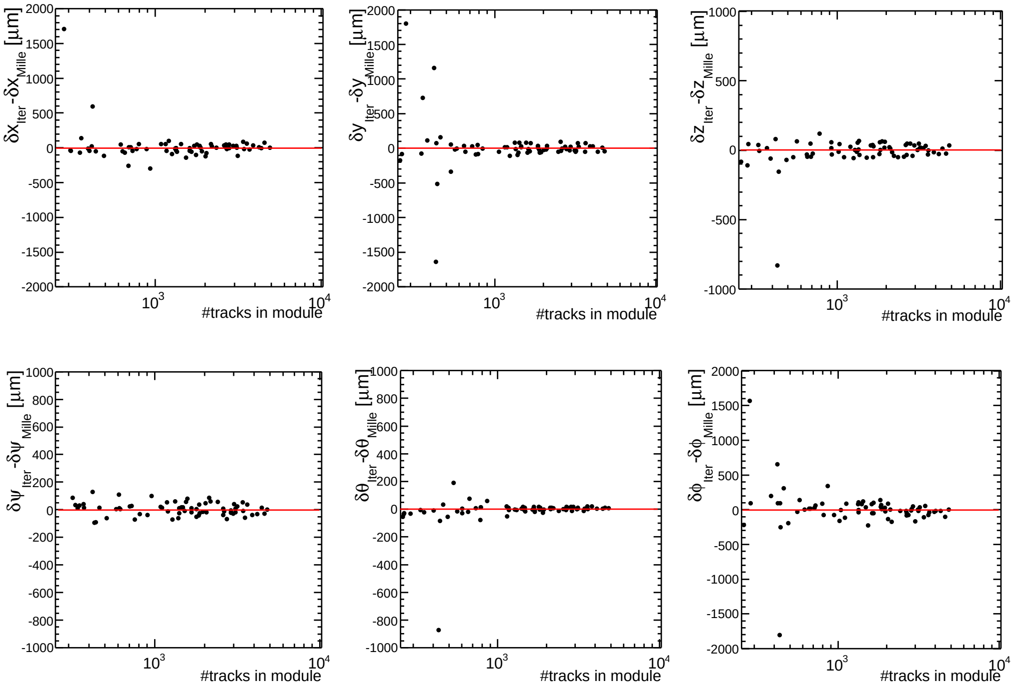

Figure 23: Difference between the alignment parameters obtained from the iterative method and Millepede, for the inner SPD layer modules, as a function of the points statistics on the module.

iterative module-by-module approach can be used for a cross-check with the Millepede algorithm, in order to further confirm the Millepede results and, since the two methods are in many aspects independent, to check the presence of possible systematic trends in the extracted alignment parameters. In Fig. 22 the values of the parameters obtained with the iterative method are plotted as a function of those obtained with Millepede. A correction was applied to account for a possible global roto-translation of the whole ITS, which does not affect the quality of the alignment and can be different for the two methods. Most of the modules are clustered along the diagonal lines, that correspond to the situation in which the parameters from the two methods are exactly the same. There are some outlier modules, that are far from the ideal result. However, the plots of the difference between the two parameter values as a function of the statistics on the module (Fig. 23) show that the outliers mostly correspond to modules with low statistics (sides of the SPD barrel).

8 Conclusions

The results on the first alignment of the ALICE Inner Tracking System with cosmic-ray tracks, collected in 2008 in the absence of magnetic field, have been presented.

The initial step of the alignment procedure consisted in the validation of the survey measurements for the Silicon Strip Detector (SSD). The three methods applied to this purpose indicate that the residual misalignment for modules on ladders is within 5 μm, i.e. negligible with respect to the intrinsic resolution of this detector in the most precise direction, while the residual misalignment for the ladders with respect to the support cones amounts to about 20 μm.

The procedure continues with track-based software alignment performing residuals minimization. We presented the results obtained with a sample of about 10^5 cosmic-ray tracks, reconstructed in events selected by the FastOR trigger of the Silicon Pixel Detector (SPD). We mainly use the Millepede algorithm, which minimizes a global χ^2 of residuals for all alignable volumes and a large set of tracks.

We start from the SPD, which is aligned in a hierarchical approach, from the largest mechanical structures (10 support sectors) to the 240 single sensor modules. About 90% of the latter were active during the 2008 cosmic run, and about 85% had enough space points (> 50) to allow the alignment. Then, we align the SPD barrel with respect to the SSD barrel. The SSD coverage provided by the cosmic-ray tracks is insufficient to align the SSD at the level of ladders, especially for the ladders close to the horizontal plane $y = 0$. Therefore, for the time being we only align the SSD at the level of large sets of ladders. The two intermediate ITS layers, the Silicon Drift Detectors (SDD), represent a special case, because the reconstruction of one of the two local coordinates requires dedicated calibration procedures (drift velocity and drift time zero extraction), which are to some extent related to the alignment. Indeed, one of the approaches that we are developing for the time zero calibration is based on the analysis of track residuals in a standalone procedure, initially, and then directly within the Millepede algorithm. Once these procedure will become stable and robust, the SDD will be included in the standard alignment chain. For all six layers, the completion of the alignment for all modules will require tracks from proton–proton collisions; a few 10^6 events (collected in a few days) should allow us to reach a uniform alignment level, close to the target, over the entire detector.

We use mainly two observables to assess the quality of the obtained alignment: the matching of the two half-tracks produced by a cosmic-ray particle in the upper and lower halves of the ITS barrel, and the residuals between double points produced in the geometrical overlaps between adjacent modules. For the SPD, both observables indicate an effective space point resolution of about 14 μm in the most precise direction, to be compared to about 11 μm extracted from the Monte Carlo simulation without misalignments. This difference of $\approx$ 25% (from 11 to 14 μm) is already quite close the 20%, which is the final target of the alignment. In addition, the measured incidence angle dependence of the spread of the double points residuals is well reproduced by Monte Carlo simulations that include random residual misalignments with a gaussian sigma of about 7 μm. Further confidence on the robustness of the results is provided, to some extent, by the cross-checks we performed using a small data set with magnetic field switched on and, mainly, by the comparison of the Millepede results to those from a second, independent, alignment method. This second method, which iteratively minimizes a set of local module-by-module χ^2 functions, yields, compared to Millepede, a similar alignment quality and a quite compatible set of alignment corrections.

Using the present data set with magnetic field off, since the track momenta are not known, the multiple scattering effect, which is certainly not negligible, cannot be disentangled from the residual misalignment effect. Therefore, a more conclusive statement on the SPD residual misalignment will be possible only after the analysis of cosmic-ray data collected with magnetic field switched on. The same applies for combined tracking with SPD, SDD and SSD points: in this case, the momentum-differential analysis of the transverse distance between the two half-tracks (upper and lower half-barrels) will allow us to measure the track transverse impact parameter resolution, which is a key performance figure in view of the ALICE heavy flavour physics program.

Acknowledgements

We thank F. Antinori, I. Belikov, P. Giubellino, G. Martinez, V. Manzari, G. Nooren and F. Tosello for fruitful discussions and comments on the manuscript, R. Dima, B. Giraudo and J.-F. Grosse Oetringhaus for providing some of the detector drawings shown in Section 2. The results presented in this note were obtained using the data collected during the 2008 cosmic-ray global run of ALICE. We are grateful to the ALICE Collaborators involved in the ITS detector construction and commissioning and in the online and offline activities related to the collection and reconstruction of the data. A shorter version of this manuscript will be proposed to the ALICE Editorial Board for publication in a scientific journal, and it will be signed by all the ALICE Collaborators directly or indirectly involved.

References

[1] K. Aamodt et al. [ALICE Collaboration], JINST 3 (2008) S08002.

[2] F. Carminati et al. [ALICE Collaboration], J. Phys. G 30 (2003) 1517, chapter 1 and references therein.

[3] U. Heinz and M. Jacob, arXiv:nucl-th/0002042, and references therein;
I. Arsene et al. [BRAHMS Collaboration], Nucl. Phys. A757 (2005) 1;
K. Adkox et al. [PHENIX Collaboration], Nucl. Phys. A757 (2005) 184;
B.B. Back et al. [PHOBOS Collaboration], Nucl. Phys. A757 (2005) 28;
J. Adams et al. [STAR Collaboration], Nucl. Phys. A757 (2005) 102.

[4] B. Alessandro et al. [ALICE Collaboration], J. Phys. G 32 (2006) 1295.

[5] V. Blobel and C. Kleinwort, contribution to the Conference on Advanced Statistical Techniques in Particle Physics, Durham, March, 18–22, 2002.

[6] ALICE Off-line framework, AliRoot, http://aliceinfo.cern.ch/Offline

[7] ROOT, http://root.cern.ch

[8] R. Grosso, in “Proceedings of the first LHC detector alignment workshop”, CERN, September 4–6, 2006, CERN-2007-004.

[9] S. Beole et al., Nucl. Inst. and Meth. A582 (2007) 733.

[10] A. Rashevsky et al., Nucl. Inst. and Meth. A572 (2007) 125.

[11] G. Batigne et al., JINST 3 (2008) P06004.

[12] S. Blusk, et al. “Proceedings of the first LHC detector alignment workshop”, CERN, September 4–6, 2006, CERN-2007-004.

[13] B.S. Nilsen et al., Nucl. Inst. and Meth. A599 (2009) 176.

[14] M. Chemarin et al. [L3 Collaboration], Nucl. Phys. Proc. Suppl. 85 (2000) 361.

[15] E. Crescio et al., ALICE Internal Note in preparation.

[16] M.G. Poghosyan et al., ALICE Internal Note in preparation.

[17] A. Dainese et al., ALICE Internal Note in preparation.

[18] V. Blobel, in “Proceedings of the first LHC detector alignment workshop”, CERN, September 4–6, 2006, CERN-2007-004.

[19] R.A. Frazer, W.J. Duncan and A.R. Collar. Elementary Matrices and Some Applications to Dynamics and Differential Equations, Cambridge University Press, Cambridge (1938).

[20] C. Paige and M. Saunders, SIAM J. Numer. Anal. 12 (1975) 617.

[21] Y. Saad and M.H. Schultz, SIAM J. Sci. Stat. Comput., 7 (1986) 856.

[22] I.S. Duff, A.M. Erisman and J.K. Reid, Direct methods for sparse matrices, Oxford University Press, London (1986).

[23] G.E. Bruno et al., ALICE Internal Note 2005-011 (2005).

[24] G.E. Bruno et al., ALICE Internal Note 2005-022 (2005).

[25] P. Brückman de Renstrom, in “Proceedings of the first LHC detector alignment workshop”, CERN, September 4–6, 2006, CERN-2007-004.

[26] F.-P. Schilling, in “Proceedings of the first LHC detector alignment workshop”, CERN, September 4–6, 2006, CERN-2007-004.

[27] V. Karimaki et al., CMS Note 2006/008 (2006).